Received: 1 April 2019 | Revised: 13 September 2019 | Accepted: 15 September 2019
DOI: 10.1002/we.2430

WILEY

RESEARCH ARTICLE

LiDAR measurements for an onshore wind farm: Wake variability for different incoming wind speeds and atmospheric stability regimes

Lu Zhan | **Stefano Letizia** | **Giacomo Valerio Iungo**

Wind Fluids and Experiments (WindFluX) Laboratory, Mechanical Engineering Department, The University of Texas at Dallas, Richardson, Texas

Correspondence
Giacomo Valerio Iungo, 800 West Campbell Rd, Richardson, TX 75080-3021, USA.
Email: valerio.iungo@utdallas.edu

Funding information
National Science Foundation, CBET, Fluid Dynamics, Grant/Award Number: 1705837; National Science Foundation, Collaborative Research: I/UCRC for Wind Energy, Science, Technology, and Research, Grant/Award Number: IIP-1362022

Abstract

Wind measurements were performed with the UTD mobile LiDAR station for an onshore wind farm located in Texas with the aim of characterizing evolution of wind-turbine wakes for different hub-height wind speeds and regimes of the static atmospheric stability. The wind velocity field was measured by means of a scanning Doppler wind LiDAR, while atmospheric boundary layer and turbine parameters were monitored through a met-tower and SCADA, respectively. The wake measurements are clustered and their ensemble statistics retrieved as functions of the hub-height wind speed and the atmospheric stability regime, which is characterized either with the Bulk Richardson number or wind turbulence intensity at hub height. The cluster analysis of the LiDAR measurements has singled out that the turbine thrust coefficient is the main parameter driving the variability of the velocity deficit in the near wake. In contrast, atmospheric stability has negligible influence on the near-wake velocity field, while it affects noticeably the far-wake evolution and recovery. A secondary effect on wake-recovery rate is observed as a function of the rotor thrust coefficient. For higher thrust coefficients, the enhanced wake-generated turbulence fosters wake recovery. A semi-empirical model is formulated to predict the maximum wake velocity deficit as a function of the downstream distance using the rotor thrust coefficient and the incoming turbulence intensity at hub height as input. The cluster analysis of the LiDAR measurements and the ensemble statistics calculated through the Barnes scheme have enabled to generate a valuable dataset for development and assessment of wind farm models.

KEYWORDS
LiDAR, wake, wind farm, wind turbine

1 | INTRODUCTION

The recent worldwide outbreak of wind power production poses new challenges for wind farm designers seeking optimal layout and control strategies to maximize profitability of wind power plants.[1,2] A considerable factor for power losses and increased fatigue loads in large wind farms is connected with wake interactions,[3-6] which are affected by farm layout, turbine settings, site topography, and are highly variable with the static stability of the atmospheric boundary layer (ABL).[7-9] Furthermore, the increasing size of wind turbine rotors[10,11] exacerbates underperformance due to wake interactions as a consequence of the increased wake extent and, in turn, the longer downstream distance required for wake recovery.

Continuous improvements in remote-sensing techniques, aiming to measure wind atmospheric turbulence, have been leveraged to achieve a deeper understanding of ABL flows[12-14] and to investigate the evolution of wakes produced by utility-scale wind turbines.[15-18] One of the first campaigns performed with light detection and ranging (LiDAR) systems with the goal of measuring wind-turbine wakes took place at a site near the coast of the northern part of Germany to probe reduction of the wind speed at certain distances downstream of a wind turbine rotor.[19] Since then, a wide range of scanning techniques has been developed for both ground- and nacelle-based LiDAR measurements of isolated wind turbines,[20-23] multiple wakes, and wake interactions.[24-27] LiDAR wake measurements were performed in the presence of yaw misalignment of the turbine rotor[28] or wind veer,[29] which induce a departure of the wake cross-section from roughly axisymmetric shape, even removing the

The peer review history for this article is available at https://publons.com/publon/10.1002/we.2430.

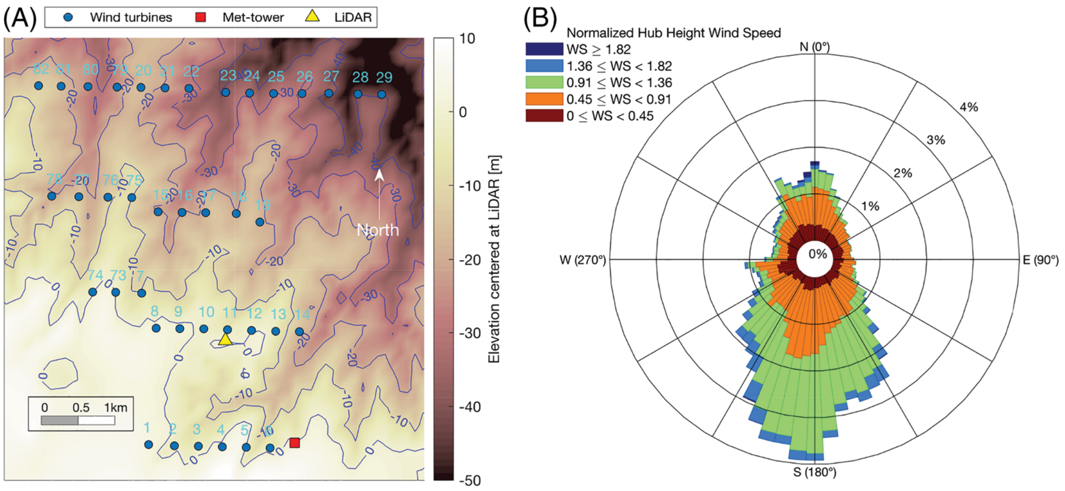

FIGURE 1 Characterization of the test site: A, layout of the wind farm, where the turbine locations are represented by blue circles with downscaled diameter of 1 *D* (relative altitude with respect to the light detection and ranging [LiDAR] location is reported over the contour lines in meters); B, wind rose of the hub-height wind measured by the met-tower and reported as a ratio of the turbine rated wind speed

skewing effect due to the vertical shear. Doppler radars have also been used to measure wakes produced by utility-scale wind turbines.[30,31] Both experimental[32-34] and numerical investigations[35-38] have pointed out static atmospheric stability being among one of the major factors affecting the evolution of wind-turbine wakes.

The aim of this study is to provide a quantitative characterization of the evolution of wind-turbine wakes covering the broad range of typical operations, namely for different incoming wind speeds and atmospheric stability regimes. The variability in the downstream direction of the wake velocity deficit is captured through a semi-empirical model as a function of the rotor thrust coefficient and turbulent intensity of the incoming wind. This research has been conducted through a cluster analysis of about 10 000 quality-controlled LiDAR scans, which are then post-processed through ensemble statistics providing mean and standard deviation of the wake velocity field for the various clusters. Therefore, the statistics of the LiDAR velocity field are calculated with high statistical accuracy, which is needed to develop and assess numerical models of wind-turbine wakes.

To investigate downstream evolution of wind-turbine wakes for different turbine settings and atmospheric stability regimes, a field campaign was carried out for an onshore wind farm located in North Texas. This experimental dataset encompasses meteorological data collected from a meteorological (met) tower, supervisory control and data acquisition (SCADA) data, and wind speed measurements collected from a scanning Doppler wind LiDAR. It is important to characterize wind-turbine wakes under realistic operative conditions, thus with a variable wind speed, thrust coefficient, and under different atmospheric stability regimes in order to enhance accuracy in prediction of wind-turbine wakes and power capture through wind farm models.[1,2,38] To this aim, LiDAR scans of wind-turbine wakes produced by wind turbines not affected by upstream wakes have been clustered according to the incoming wind speed and atmospheric stability regime. For each cluster, mean and standard deviation of the streamwise velocity field have been calculated through ensemble statistics enabling the characterization of the wake development for different atmospheric stability regimes and turbine settings. For this work, the wind farm under examination is installed over a flat terrain. However, the cluster analysis of LiDAR data is suitable for LiDAR measurements carried out in complex terrain as well, by including parameters that enable the detection of flow distortions induced by the site topography, such as wind direction, turbine location, and Froude number.[39]

The remainder of the paper is organized as follows: in Section 2, the experimental setup and the test site are described. Sections 3 and 4 report in detail the procedure for the post-processing and clustering, respectively, of single-wake LiDAR scans. In Section 5, ensemble statistics of plan position indicator (PPI) scans belonging to the same cluster are retrieved through the Barnes scheme.[40,41] In Section 6, average and standard deviation of the wake velocity field are investigated for different hub-height wind speed and atmospheric stability regimes. Concluding remarks are then reported in Section 7.

2 | SITE AND EXPERIMENTAL SETUP

A field campaign was performed for an onshore wind farm located in North Texas consisting of identical 2.3-MW wind turbines with rotor diameter, *D*, of 108 m, and hub height of 80 m. The elevation map of the site, which is plotted on the background of Figure 1A, is retrieved with a spatial resolution of 100 m from the US Geological Survey.[42] By setting the offset altitude at the location of the LiDAR deployment, the standard deviation of the topography is of only 16 m, which allows considering this site as a flat terrain. For the retrieval of the LiDAR data, the hub height of each turbine is corrected by taking the local altitude at the turbine locations into account.

The measurement campaign was conducted through various phases between August 2015 and March 2017 for a total of 236 days. The wind rose for this site was obtained from meteorological data collected at hub height for the entire duration of the experiment from a met-tower

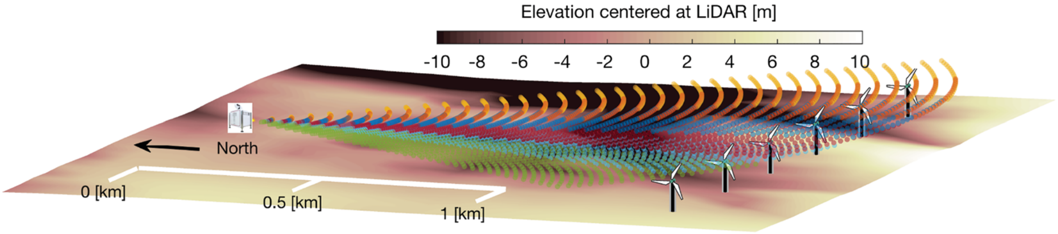

FIGURE 2 Sketch of the area probed with the light detection and ranging (LiDAR) plan position indicator (PPI) scans and relative position of the wind turbines under investigation. The LiDAR samples are colored according to the different PPI scans

located at the south-east corner of the farm (Figure 1A). From the wind rose reported in Figure 1B, it is evident the occurrence of a prevailing southerly wind direction, which allows classifying this wind farm in four rows: row 1 with turbines 1 to 6, row 2 with turbines 7 to 14 and 73 and 74, row 3 with turbines 15 to 19 and 75 to 78, and row 4 with turbines 20 to 29 and 79 to 82. The streamwise distance between turbine rows for the prevailing southerly wind directions is about 14 *D*. Meteorological data were provided at various heights as 10-minute averages and standard deviation of wind speed (at 36, 60, and 80 m), wind direction (at 36, 60, and 80 m), temperature (at 3 and 75 m), humidity (at 3 and 75 m), and barometric pressure (at 2 and 75 m).

SCADA data were provided for each turbine as 10-minute averages and standard deviation of wind speed, power output, rotor rotational velocity, and yaw angle. These data are used to calculate power curves for the various wind turbines according to the International Electrotechnical Commission (IEC) standard[43] as well as to assess parameters retrieved from the LiDAR measurements. For more details on this dataset and the used quality control process, see El-Asha et al.[9]

The wind velocity around and within the turbine array was measured with a Windcube 200S manufactured by Leosphere, which is a scanning Doppler wind LiDAR embedded in the UTD mobile LiDAR station to allow easy deployment, control, data collection, and monitoring of the instrument.[9] This LiDAR is characterized by a typical scanning range of 4 km with a range gate between 25 and 100 m, accumulation time of 500 ms, and azimuth and elevation capabilities of 0° to 360° and -10° to 190° , respectively. The deployment location of the LiDAR is shown in Figure 1A with a yellow triangle.

A scanning Doppler wind LiDAR measures the radial (also denoted as line-of-sight) velocity, which is the sum of the projections of the three Cartesian wind velocity components in the direction of the LiDAR laser beam. According to the wind farm layout and the prevalence of southerly wind directions (Figure 1 B), for wind directions within the sector 145° and 235°, the wakes produced by the turbines from 1 to 6 evolve roughly towards the LiDAR location, which is a favorable condition for the LiDAR to measure with close approximation the streamwise velocity through single-wake PPI scans.

The specific scan parameters were selected according to the actual distance between the LiDAR and the turbine under examination, aerosol, and atmospheric conditions. Main constraints in the selection of the scan parameters consisted in achieving a carrier-to-noise ratio (CNR) higher than −25 dB throughout the range of interest in order to ensure an accuracy in the velocity measurements higher than 0.5 m s^{-1},[14,22,44] and acquisition of measurements at hub height within the downstream range 1 to 3 *D* with at least five measurement points in the transverse direction within the wake. The main parameters of the single-wake PPI scans are summarized in Table 1. A sketch of the area probed through the LiDAR PPI scans and the relative locations of the turbines under investigation is reported in Figure 2. The typical range gate adopted for the LiDAR measurements was 50 m, seldom it was reduced to 25 m or increased to 75 m in presence of very favorable or disadvantageous, respectively, aerosol conditions. The typical LiDAR elevation angle was between 2° and 5°, which allowed, as it will be detailed in the following, achieving a good approximation of the horizontal wind speed from the LiDAR radial velocity.

The rotation speed of the scanning head in the azimuthal direction was adjusted between 1° s^{-1} and 2° s^{-1}, depending on wind and atmospheric conditions. Through preliminary measurements, it was observed that the downstream evolution of the wakes did not show significant meandering-like oscillations under stable atmospheric conditions[45,46]; thus, a relatively slow rotation speed of 1° s^{-1} was used together with a relatively narrow azimuthal range of 10° . This scan is characterized by a sampling time of about 10 seconds, angular resolution of 0.5° , which corresponds to a transverse resolution of about 15 m at the turbine location. Under convective atmospheric regimes, wider azimuthal ranges were needed in order to capture the meandering-like oscillations within the measurement area (up to 20°), which required, in turn, a higher rotation speed of 2 ° s^{-1} in order to keep the sampling time approximately equal to 10 seconds. The single-wake PPI scans were typically performed with raster mode, namely by reversing the LiDAR rotation speed for consecutive PPI scans in order to minimize the sampling time. For this field campaign, a total number of 9888 quality-controlled single-wake PPI scans were acquired.

TABLE 1 Scanning parameters for the single-wake PPI LiDAR scans

	Rotation Speed [° s^{-1}]		Range Gate [m]			Azimuth Range (°)		Elevation (°)			Max. Sampling Time (s)	
Value	1	2	25	50	75	10	20	2-3	3-4	4-5	10	20
Occurrence	27%	73%	2.5%	96%	1.5%	22%	78%	7.5%	77%	15.5%	95%	5%

Abbreviations: LiDAR, light detection and ranging; PPI, plan position indicator.

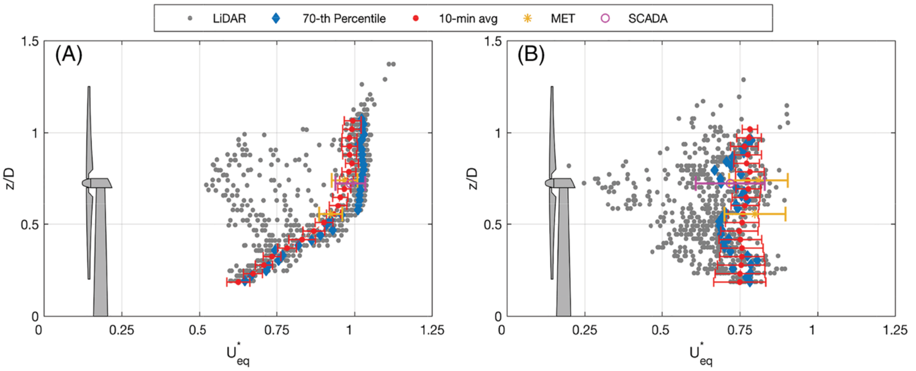

FIGURE 3 Estimation of the vertical profile of the incoming wind speed, U_∞: A, August 2, 2016, 2:19 AM local time, stable ABL with TI = 4.8%; B, August 2, 2016, 12:41 PM local time, unstable ABL with TI = 18%. Blue diamonds represent values of the 70-th percentile of the LiDAR equivalent velocity (gray circles), while the red circles indicate 10-minute average of the values obtained through the 70th percentile from consecutive scans. Respective meteorological (in gold) and supervisory control and data acquisition (SCADA) data (in pink) are also reported. Error bars represent standard deviation

3 | POST-PROCESSING OF SINGLE-WAKE PPI SCANS

The radial velocity, V_r, measured by the LiDAR can be expressed as

$$V_r = V_h \quad cos\phi \;\; cos(\theta - \theta_w) + W \; sin\phi, \tag{1}$$

where ϕ and θ are the elevation and azimuth angles, respectively, of the LiDAR laser beam, θ_w is the local wind direction, and V_h and W are the horizontal and vertical velocity components, respectively. The last term on the right-hand-side of Equation (1) is practically negligible considering the small elevation angles used for these LiDAR measurements (Table 1) and the typical small values of the vertical velocity, W, compared with those of the horizontal wind speed, V_h.[15,47,48] Assuming a constant wind direction, θ_w, over each PPI plane and equal to the average direction of the wake advection, we can then calculate the streamwise equivalent velocity, U_{eq}, as follows:

$$U_{eq} \sim V_r \quad / \quad [cos\phi \;\; cos(\theta - \theta_w)]\,, \tag{2}$$

which represents a proxy for the horizontal streamwise velocity and it is the most relevant velocity component for characterizing wake features. To strengthen the assumption of a uniform θ_w for each PPI scan, measurements acquired during the occurrence of wind veer larger than 10° between 36 and 80-m heights (occurrence of 0.6% over the entire dataset) have been excluded for this investigation.

U_{eq} is interpolated from the spherical coordinates of the LiDAR measurements to a Cartesian reference frame whose origin is fixed at the turbine hub, x-direction pointing downstream in the wake direction, θ_w, z-direction oriented vertically and pointing upwards, and the y-direction is in the transverse direction in order to produce a right-handed reference frame. For estimating θ_w, the wind velocity field is reported over a structured grid with a resolution of 0.25 D in the streamwise direction within the range from 1 to 10 D while the transverse spatial resolution is of 0.2 D within the range ± 1.5 D.

In order to remove the effects of wind variability on the ensemble statistics of the wake measurements, the velocity fields are normalized by the incoming vertical profile of the horizontal wind speed for the respective PPI scan, as follows:

$$U^*_{eq}(x, y, z) = \frac{U_{eq}(x, y, z)}{U_\infty(z)}. \tag{3}$$

Classical LiDAR scans to probe the ABL vertical profile, such as the velocity-azimuth display (VAD) or Doppler beam swinging (DBS), are not applicable for these LiDAR measurements due to the presence of wakes intersecting the measurement volume and spatial variability of the ABL flow within the wind farm area. Therefore, the vertical profile of the incoming horizontal wind speed is directly calculated from the single-wake PPI scans through the value of the 70th percentile of the distribution of the streamwise equivalent velocity, U_{eq}, for each height probed by the LiDAR. The 70th percentile has been chosen through a sensitivity analysis in order to maximize the correlation between the 10-minute averaged LiDAR measurements with the measurements of the met-tower at hub height (Pearson correlation coefficient, $\rho = 0.972$) and SCADA data ($\rho = 0.977$). An example of the estimate of the ABL velocity profile from PPI scans is provided in Figure 3. It can be observed how the selected value of the 70th percentile represents a good trade-off to filter out turbulent gusts while removing effects of LiDAR samples with reduced wind speed in correspondence of the wind-turbine wake.

For the PPI scans, roughly 90% of the LiDAR samples were collected downstream of the turbine under examination within the region $0.5 \leq x/D \leq 8$ and within a vertical range of $z/D = \pm 0.25$. Therefore, LiDAR samples of the streamwise equivalent velocity can be considered as representative of the wake velocity field at hub height. For the analysis of the wake velocity fields, the wake center is always considered at hub height, while each LiDAR sample is reported as a function of its downstream location, x, and radial distance from the estimated wake center at

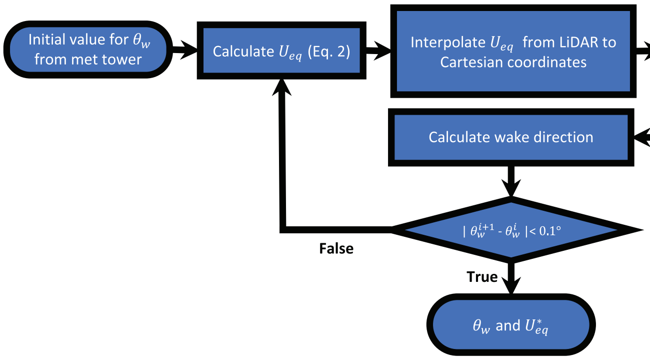

FIGURE 4 Flowchart for the post-processing of the light detection and ranging (LiDAR) data

the respective downstream position, with sign in order to differentiate the two sides of the wake,

$$r = \frac{(y - y_c)}{|y - y_c|} \sqrt{(y - y_c)^2 + z^2}, \tag{4}$$

where y_c is the transverse coordinate of the wake center.

For each PPI scan, the calculation of U_{eq}^* requires the estimate of the wake direction, which is ideally equal to the local mean wind direction at the rotor disk; however, noticeable angular differences can be observed between the analysis of the LiDAR wake measurements and wind data collected from the met-tower and SCADA data. The mean wind direction is monitored through the wind vanes installed over the met-tower and the yaw angle of the individual turbines, which is recorded by the SCADA. While the former might not be representative for the local wind direction at specific turbine locations due to spatial variability of the wind field, the latter is recorded with a low sampling rate of 10 minutes and it might differ from the incoming wind direction in presence of a significant wind veer.[29] Although cases with evident wind veer are excluded for this data analysis, even small errors in the estimate of the wake direction can lead to inaccurate characterizations of the wake recovery.

Wind direction measured by the met-tower at height of 75 m is utilized as first attempt to estimate θ_w and, in turn, U_{eq}^* is calculated through Equations 2 and 3. The wake direction is then updated as the direction of the line fitting the wake centers estimated at the various downstream locations probed by the LiDAR. This new value of θ_w is used to recalculate U_{eq} and U_∞, and this procedure is iteratively advanced until convergence is achieved in θ_w with an accuracy of 0.1°. A flowchart illustrating the different steps involved in the calculation of U_{eq}^* and θ_w is reported in Figure 4.

To estimate the transverse location of the wake center from each PPI scan, we performed the fitting of U_{eq}^* at a given downstream location with a Gaussian function[21,49] as follows:

$$G(r, r_c, \sigma, \Delta U) = 1 - \Delta U \cdot exp\left(-\frac{(r - r_c)^2}{2\sigma^2}\right), \tag{5}$$

where ΔU is the maximum nondimensional velocity deficit at the considered downstream location, r_c is the radial position of the wake center at a given downstream location, and σ is the standard deviation of the Gaussian function characterizing the wake width. All these parameters are obtained from the least-squares regression of the LiDAR measurements at a given downstream location with Equation 5. The quality of the fitting of the wake velocity profiles is controlled through the mean-square deviation and a threshold equal to 10% of U_∞ at hub height is used to reject scans with poor accuracy in the fitting.

Once the wake centers are estimated for the various downstream locations, the updated wake direction, θ_w, is then obtained through a weighted linear fitting of the wake centers with a weighting function calculated as $w(x) = x^{-\beta}$, where the exponent β decreases among integer values from 4 to 0 for consecutive iterations. This weighting function is introduced to stabilize the numerical procedure and to enhance the significance of the near-wake centers for the first iterations in the estimate of θ_w. In Figure 5, the histogram of the $R - square$ value of the fitting of the wake velocity field with Equation 5 at each downstream location and all the PPI scans is reported. The mean and median values of $R - square$ are 0.878 and 0.934, respectively, indicating the good accuracy achieved in fitting the wake velocity field with a Gaussian function and in detecting the wake centers. Few outliers with low $R - square$ value are seldom observed for downstream locations larger than 6 D and, thus, having negligible effect on the estimate of the wake direction due to the weighted linear fitting of the wake centers.

Since the streamwise velocity, U_{eq}, is a function of the wake direction (Equation 2), and U_{eq} is post-processed to estimate the wake direction, an iterative procedure is then implemented to estimate both U_{eq} and θ_w, which is schematically reported in the flowchart of Figure 4. Convergence of this iterative method is achieved when consecutive iterations produce a modification of θ_w smaller than 0.1°. A time-series of the instantaneous wake direction estimated for turbine 4 is reported in Figure 6. The 10-minute moving average of θ_w shows high correlation with the turbine yaw angle (average value of 0.97). Furthermore, fluctuations of θ_w are observed within each 10-minute period with standard deviation roughly proportional to the wind turbulence intensity, which suggests these fluctuations being associated with the incoming atmospheric turbulence.

4 | CLUSTERING OF SINGLE-WAKE PPI SCANS

Once the wake velocity fields are expressed in terms of nondimensional streamwise equivalent velocity, U_{eq}^*, and each sample reported in a common reference frame with x-direction equal to the wake direction of its respective PPI scan, it is possible to calculate ensemble statistics of

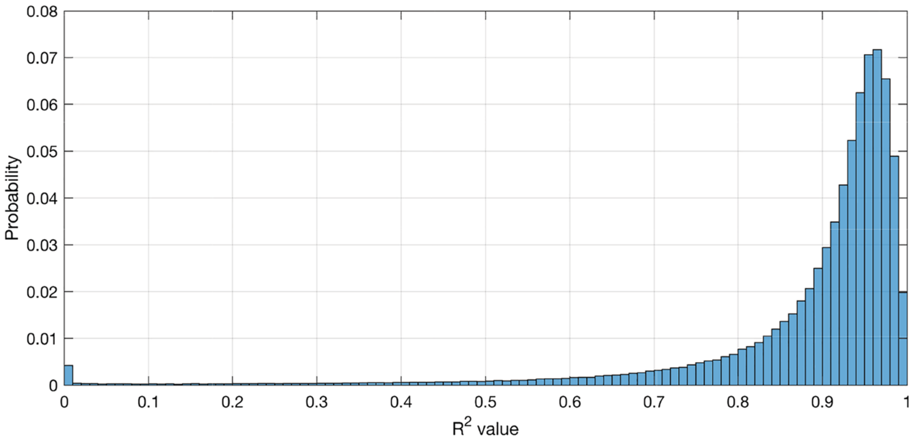

FIGURE 5 Histogram of the $R-square$ value for the fitting of U_{eq}^{*} with Equation 5 calculated at each downstream location and for all the quality-controlled plan position indicator (PPI) scans

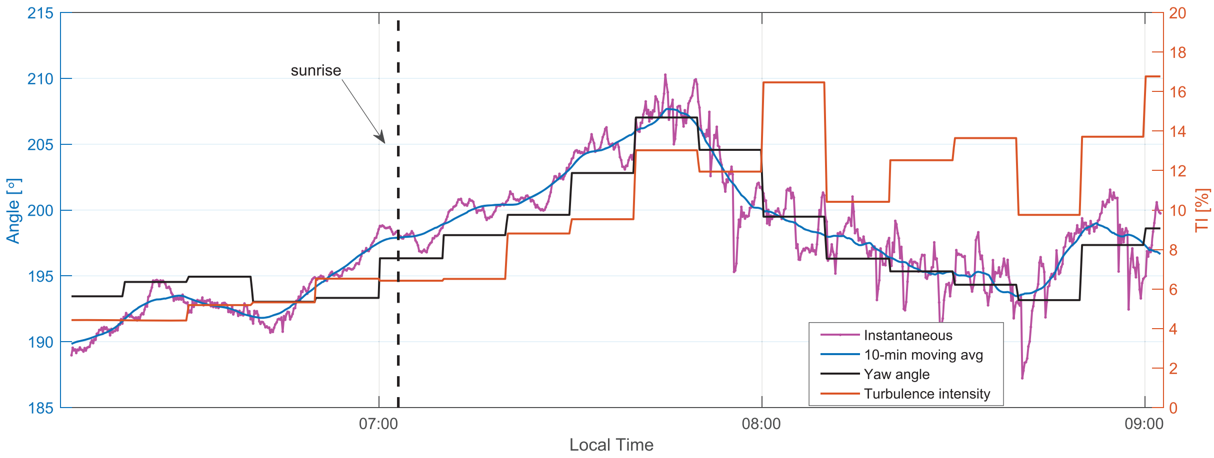

FIGURE 6 Estimate of the wake direction, θ_w, for turbine 4: instantaneous and 10-minute moving average of the wake direction compared with supervisory control and data acquisition (SCADA) yaw angle and wind turbulence intensity on August 10, 2016

the wake velocity field. LiDAR data are clustered in order to characterize the wake variability for different turbine settings and wake evolution affected by the atmospheric stability. LiDAR data are first clustered as a function of the incoming wind speed at hub-height, which is corrected for the variation of air density as recommended by the IEC standard[43] as follows:

$$U_{hub}^{corr} = U_{hub}\left(\frac{\rho_{10min}}{\rho_0}\right)^{1/3}, \tag{6}$$

where U_{hub} is the 10-minute averaged wind speed measured from the SCADA, ρ_{10min} is the 10-minute averaged air density calculated through temperature and pressure data recorded from the met-tower, and ρ_0 is the reference air density of 1.225 kg m^{-3}. In order to characterize turbine operations, the hub height wind speed normalized by the turbine-rated wind speed, U_{hub}^{*}, is deemed being a good parameter to monitor variability of the thrust force induced by the turbine rotor.

Figure 7A shows power capture of the six turbines under examination normalized by the rated power as a function of U_{hub}^{*}. It is noteworthy that for operations above the rated wind speed, namely in region 3 of the power curve, a power boost controller can be activated allowing increase of the rated power of about 5% of its nominal value. The power boost is activated only under specific conditions of the ambient temperature, main component temperature, turbulence level, and grid voltage levels.

Figure 7B shows the blade pitch angle for different values of the incoming wind speed and highlights the transition from regions 2 to 3 at U_{hub}^{*} about 0.71, where the pitch controller gradually increases the blade pitch angle in order to reduce the thrust coefficient of the blades while limiting power capture to rated value. Several outliers are observed in Figure 7B, especially transitioning from regions 2 to 3 of the power curve, which might be related to specific tasks of the turbine controller. In Figure 7C, the power curve is obtained by performing bin averaging of the SCADA data with bin width of 0.5 $m\,s^{-1}$ (0.045 normalized with rated wind speed) based on the IEC standard.[43] The C_t curve is estimated from induction factor and power coefficient with 1-D stream-tube assumption.[48] The induction factor, a, is calculated from the equation $C_p = 4a(1-a)^2$, which is then plugged in the following relationship to retrieve the thrust coefficient:

$$C_t = 4a(1-a). \tag{7}$$

For each cluster, the number of PPI scans should be large enough in order to represent wake evolution as an ergodic process. Therefore, convergence of mean and standard deviation of the wake velocity fields is checked by gradually increasing the number of PPI scans belonging to the same cluster. On the other hand, the cluster width should be small enough in order to characterize variability of C_p and C_t as a function of the incoming wind speed (Figure 7C). Based on a sensitivity analysis of mean and standard deviation of the wake velocity fields, the following values of the normalized wind speed have been selected as edges of the various clusters, which are reported in Figure 7: 0.35, 0.44, 0.53, 0.62, 0.71, 0.76, 0.8, 0.85, 0.90, 0.95, 1.00, 1.04, 1.1, and 1.14.

Subsequently, each cluster of the LiDAR data based on U^*_{hub} has been further divided into subclusters as a function of atmospheric stability regime, which strongly affects downstream evolution of wind-turbine wakes.[8,9] Atmospheric stability can be characterized through the Obukhov length, L, which, according to the Monin-Obukhov similarity theory,[47,50-52] is proportional to the height above the ground where buoyancy-produced turbulence begins dominating over shear-produced turbulence:

$$L = -\frac{T u_*^3}{k g \, \overline{w'T'}}, \tag{8}$$

where u_* is the friction velocity calculated as $u_* = \left(\overline{u'w'}^2 + \overline{v'w'}^2\right)^{1/4}$, T is the virtual potential temperature (kelvins), k is the von Kármán constant (0.4), g is the gravitational acceleration, and $\overline{w'T'}$ is the sensible heat flux. Retrieval of the Obukhov length requires high-frequency temperature and 3-D velocity measurements within the surface layer. For this field campaign, two sonic anemometers Campbell Scientific CSAT3 were installed in proximity of the LiDAR location at height of 3 m. However, the anemometer data are only available for a limited period of the campaign and never during the single-wake PPI scans. As an alternative, atmospheric stability can be characterized through the Bulk Richardson number[47,52,53] as follows:

$$Ri_B(\bar{z}) = \frac{g}{T(z_w)} \frac{\frac{\Delta T}{\Delta z}}{U^2(z_w)} \bar{z}^2 \tag{9}$$

where $z_w = 60$ m is the met-tower height where wind speed is measured, ΔT is the variation in temperature between heights $z_1 = 3$ m and $z_2 = 75$ m, and the geometric mean of these two heights is $\bar{z} = \sqrt{(z_1 z_2)} = 15$ m. Therefore, the Bulk Richardson number can directly be measured through the velocity and temperature measurements provided from the meteorological data. Ri_B can also be calculated through the stability parameter, $\bar{z}/L$, as[47]

$$Ri_B(\bar{z}) = \frac{\bar{z}}{L} \frac{\phi_H(\bar{z}/L)}{\phi_M^2(\bar{z}/L)} \tag{10}$$

through the evaluation of the nondimensional temperature and velocity functions ϕ_H and ϕ_M, respectively, which are the functional forms provided by Businger et al[54] and Dyer.[55] In Figure 8, Ri_B obtained from the stability parameter measured through the sonic anemometers (Equation (10)) is compared with that directly calculated through the meteorological data (Equation (9)). A good agreement between meteorological and sonic anemometer data is observed in the estimate of Ri_B through their linear regression in Figure 8 B (slope 0.81, intercept 0.001, and R-square value 0.67).

According to the above-presented analysis, clustering of the LiDAR wake measurements as a function of the atmospheric stability is performed through the Bulk Richardson number calculated from the meteorological data and utilizing the various stability classes suggested in the Golder's diagram[56] by considering an aerodynamic roughness length of 0.01 m, which is representative for the site under examination featured by flat grassland.[47] The various ranges of Obukhov length and Bulk Richardson number belonging to the various stability classes are reported in Table 2. It is noteworthy that although seven stability classes are envisaged, LiDAR data are unavailable for highly stable conditions (class 7) and not with

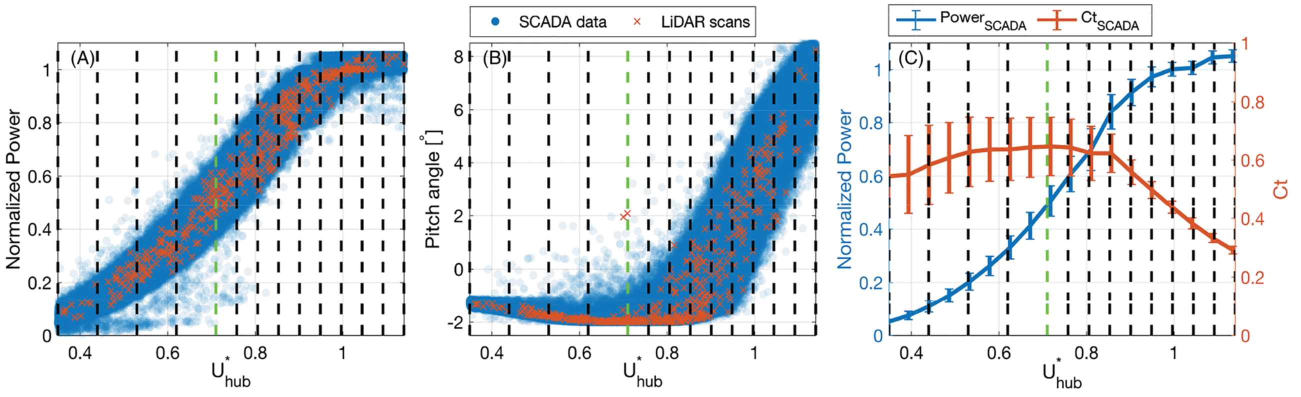

FIGURE 7 Performance characterization of the turbines 1, 2, 3, 4, 5, and 6: A, power capture normalized by the turbine rated power as a function of the normalized hub height wind speed, U^*_{hub}; B, blade pitch angle as a function of U^*_{hub}, red crosses indicate data corresponding to quality-controlled light detection and ranging (LiDAR) measurements; and C, power curve and C_t curve obtained through bin averaging. The vertical dashed black lines indicate boundaries of the various clusters based on U^*_{hub}, while the green vertical dashed lines indicate transition between regions 2 and region 3

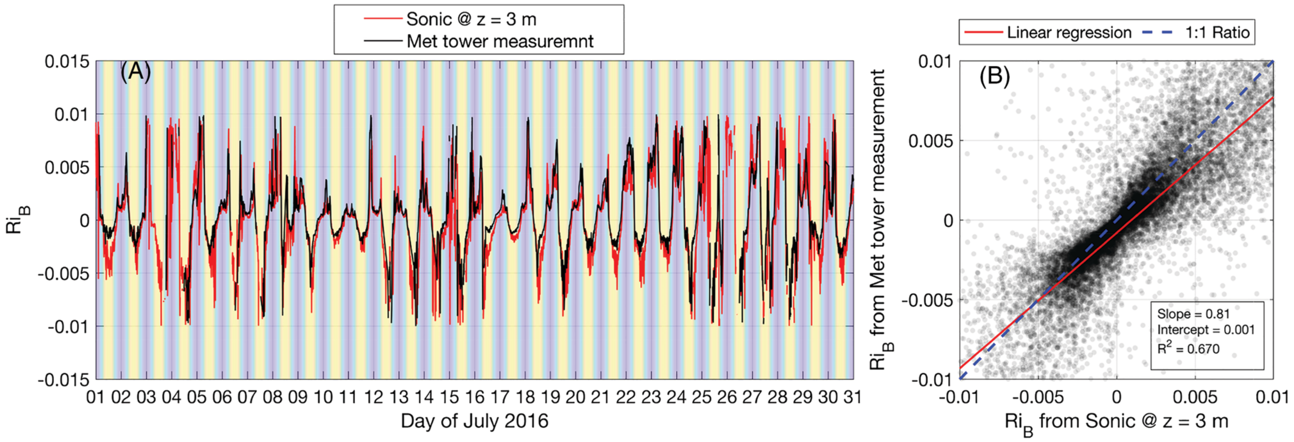

FIGURE 8 Comparison between Ri_B obtained from sonic anemometer at z = 3 m and meteorological data: A, 1-month long time-series, color in the background represents daytime (yellow) and nighttime (blue); B, scatter plot for all the sonic anemometer data available (duration approximately 6 months). Red line is the linear regression, while the blue dashed line indicates the 1:1 line

TABLE 2 Atmospheric stability classes based on the Golder's diagram[56]

Class	Obukhov Length [m]	Ri_B	Atmospheric Stability	TI range [%]
1	$-9.42 < L \leq -5.00$	$Ri_B \leq -0.0071$	Highly convective	$TI > 23.5$
2	$-15.13 < L \leq -9.42$	$-0.0071 < Ri_B \leq -0.005$	Convective	$19.4 < TI \leq 23.5$
3	$-40.45 < L \leq -15.13$	$-0.005 < Ri_B \leq -0.0024$	Weakly convective	$13.5 < TI \leq 19.4$
4	$L \leq -40.45$ or $L \geq 147.50$	$-0.0024 < Ri_B \leq 0.0011$	Neutral	$7 < TI \leq 13.5$
5	$47.14 < L \leq 147.50$	$0.0011 < Ri_B \leq 0.0033$	Weakly stable	$5.5 < TI \leq 7$
6	$17.20 < L \leq 47.14$	$0.0033 < Ri_B \leq 0.0067$	Stable	$4 < TI \leq 5.5$
7	$5.00 < L \leq 17.20$	$Ri_B > 0.0067$	Highly stable	$TI \leq 4$

a sufficient number of scans for the highly convective regime (class 1). Therefore, convective and highly convective data are merged into only one cluster for a total of five clusters based on atmospheric stability.

The calculation of the Bulk Richardson number requires temperature and velocity measurements at different heights, which are not always available for wind power plants. Therefore, as an alternative method, we propose to cluster LiDAR data for the atmospheric stability based on the turbulence intensity of the incoming wind at hub height, *TI*, which is directly calculated by the SCADA for 10-minute periods as the ratio between the standard deviation and mean value of the wind speed. Both parameters, Ri_B and *TI*, can be considered as complementary criteria to characterize the atmospheric stability; indeed, the former provides a direct comparison between the main forcing on the ABL due to atmospheric stability, namely buoyancy and shear forces, while the latter quantifies their effects on the average velocity fluctuations as a ratio with the mean wind speed. *TI* is reported as a function of Ri_B for the duration of the experiment in Figure 9. Transitioning from neutral to convective regimes, *TI* increases roughly monotonically with reducing Ri_B,[8,57-59] which makes straightforward the definition of *TI* ranges for clustering the LiDAR data as a function of atmospheric stability with a criterion equivalent to that adopted for Ri_B. However, for stable regimes, *TI* variation is very limited with Ri_B and typically confined within a range between 4% and 7%. Furthermore, for stable conditions, some outliers are observed in Figure 9

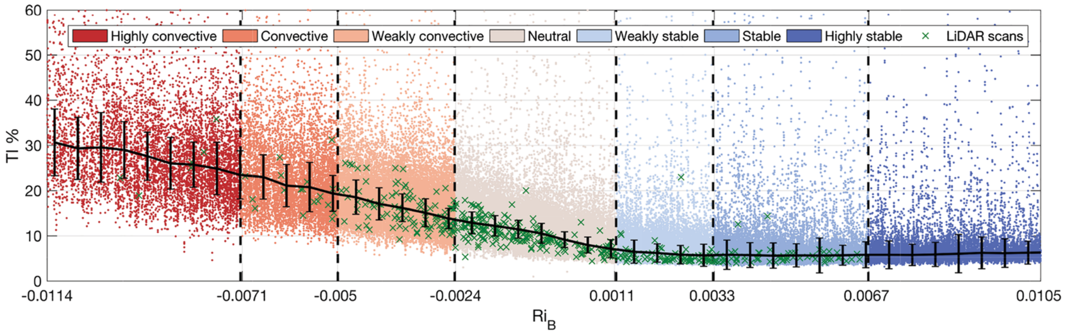

FIGURE 9 Turbulence intensity at hub height for the wind turbines under examination recorded by the supervisory control and data acquisition (SCADA) as a function of the bulk Richardson number calculated from the meteorological data. The vertical dashed black lines represent edges of the various atmospheric stability classes reported in Table 2. The green crosses indicate data corresponding to quality-controlled light detection and ranging (LiDAR) scans

with higher *TI*, which most probably correspond to passages of cold weather fronts.[60] The various classes in the stable regime are simply defined with evenly spaced ranges of *TI*, which are reported in Table 2.

5 | ENSEMBLE STATISTICS OF CLUSTERED LIDAR DATA

For each cluster produced as a function of the incoming wind speed, U^*_{hub}, and atmospheric stability regime, estimated either with Ri_B or *TI*, the LiDAR data normalized by the incoming ABL profile (Equation (3)) and reported in a reference frame with *x*-direction equal to the respective wake direction are post-processed in order to calculate their ensemble statistics. Statistically irrelevant circumstances, such as wind turbine shutdown, and occurrence of wake interactions have been discarded for the present analysis.

For each cluster of the LiDAR data, ensemble statistics are calculated with the Barnes scheme.[40,41] Grid characteristics for applications of the Barnes scheme should be defined as a trade-off between spatial resolution of the available LiDAR data and spatial variability of the wake velocity field. Considering that for wind-turbine wakes, velocity gradients in the radial direction are generally larger than those in the streamwise direction, we calculated ensemble statistics of the LiDAR data over a cylindrical domain with streamwise resolution $dx/D = 0.5$ and radial resolution of $dr/D = 0.05$. For each grid point (x_j, r_i), the average velocity field is calculated through the Barnes scheme as follows:

$$\overline{U_{eq}}(x_j, r_i) = \frac{\sum_{k=1}^{n} U^*_{eq}(x_k, r_k) w_k(x_j) w_k(r_i)}{\sum_{k=1}^{n} w_k(x_j) w_k(r_i)}, \tag{11}$$

where n is the total number of LiDAR samples falling within the grid cell with centroid (x_j, r_i) while the streamwise weighting function is given by

$$w_k(x_j) = e^{-\frac{(x_j - x_k)^2}{2\sigma_x^2}} \tag{12}$$

and the radial weighting function is

$$w_k(r_i) = e^{-\frac{(r_i - r_k)^2}{2\sigma_r^2}}. \tag{13}$$

The standard deviation of the two weighting functions is set equal to the respective grid resolutions, *dx* and *dr*, multiplied by a factor $\beta = 2$, which has been selected upon sensitivity analysis. As shown in Figure 10, a small value of β leads to a poor averaging of the velocity profiles, while larger values of β entail an excessive spatial smoothing at regions with higher velocity gradients.

According to the Barnes scheme, for each grid point, the ensemble standard deviation is calculated as follows:

$$\sigma_U(x_j, r_i) = \sqrt{\frac{\sum_{k=1}^{n} \left[U^*_{eq,k} - \overline{U_{eq}}(x_j, r_i)\right]^2 w_k(x_j) w_k(r_i)}{\sum_{k=1}^{n} w_k(x_j) w_k(r_i)}}. \tag{14}$$

The ensemble standard deviation, σ_U, encompasses velocity fluctuations associated with wake dynamics, such as meandering, turbulence, wake vortical structures,[17,61-63] and numerical errors due to the spatial variability of the mean velocity field within each grid cell.

The statistical significance of the ensemble statistics is checked by analyzing the number of LiDAR samples collected for each grid cell and through the standard error of the weighted mean (SEWM). Under the assumptions of negligible correlation among the velocity fields acquired

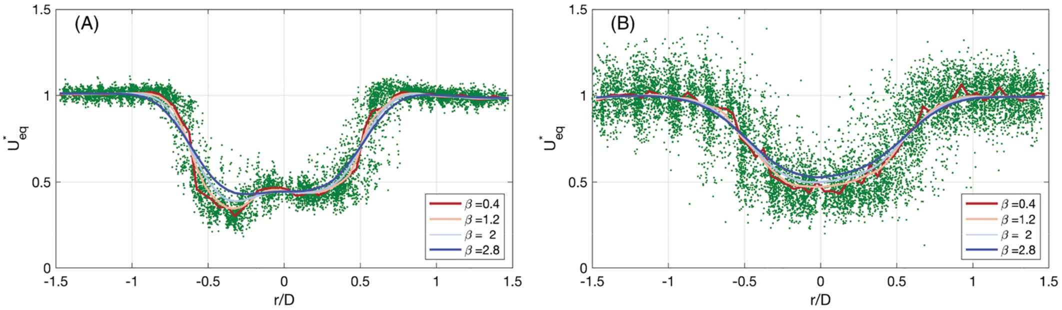

FIGURE 10 Ensemble average of the light detection and ranging (LiDAR) measurements calculated with different β values of the Barnes scheme. LiDAR data are collected at $x/D = 1.75 \pm 0.25$ for the cluster with $0.76 < U^*_{hub} \leq 0.80$ and different TI: A, $4\% < TI \leq 5.5\%$; B, $13.5\% < TI \leq 19.4\%$

through the various PPI scans and uniform uncertainty of the samples within each cell, the SEWM reads

$$\sigma_{<U>} = \sigma_U \sqrt{\sum_{k=1}^{n} \left(\frac{w_k(x_j) w_k(r_i)}{\sum_{k=1}^{n} w_k(x_j) w_k(r_i)} \right)^2}. \tag{15}$$

For our analysis, grid points with $\sigma_{<U>}$ larger than 0.8% are rejected in order to ensure an adequate accuracy in the analysis of the wake velocity field for different clusters. The threshold value of $\sigma_{<U>} = 0.8\%$ has been selected upon sensitivity analysis on the wake statistics and number of rejected LiDAR samples.

The above-presented statistical parameters are reported in Figure 11 for the cluster with normalized incoming wind speed between 0.71 and 0.76 and *TI* between 13.5% and 19.4%. In Figure 11A, the ensemble average of the streamwise velocity field clearly shows the presence of the wake velocity deficit generated by the turbine rotor and wake recovery in the downstream direction. Grid points without any LiDAR sample are left blank in Figure 11. Blank statistics typically occur in proximity of the wake center with increasing downstream distances due to the inclination of the PPI plane and for lateral downstream locations due to the misalignment between the wake direction and the direction connecting the location of the turbine under examination and the LiDAR location. In other words, the turbine wakes can cross the LiDAR measurement plane with a certain yaw angle leading to nonsymmetric distribution of the LiDAR samples (Figure 11C).

In Figure 11B, the standard deviation of the streamwise velocity field highlights the typical higher velocity fluctuations in proximity of the wake boundary, which reduce by proceeding downstream, as already documented through previous wind tunnel experiments[61,62,64] and numerical simulations.[65,66] As mentioned above, the ensemble statistics need to be filtered in order to ensure statistical significance for the various clusters of the LiDAR data. To this aim, the number of LiDAR samples for each grid cell (Figure 11C) is analyzed together with the SEWM (Figure 11D). The iso-curve with a value equal to the selected threshold of SEWM = 0.8% is reported in Figure 11 as a black dashed line. The region with high SEWM singled out for $x/D > 4$ and $r/D < 0$ is clearly related to the small number of LiDAR samples collected in that wake region, as shown in Figure 11C. Other two regions with high SEWM and, thus, reduced statistical accuracy are detected in proximity of the wake boundaries in the near-wake. This statistical feature is due to the lower number of samples acquired in the near wake and also to the enhanced velocity fluctuations occurring in that region, as highlighted by the velocity standard deviation reported in Figure 11B. These enhanced velocity fluctuations are most probably due to the detachment of wake vortical structures from the turbine rotor.[17,61-63] Statistics at grid points with rejected values are interpolated with the Matlab function inpaint_nans.[67] This function interpolates NaN elements of a 2-D array by applying a ∇^4 operator to the non-NaN elements and performing a least-squares interpolation for the points of interest.

In Figure 12, wake profiles calculated along the transverse direction at different downstream locations are reported in terms of mean and standard deviation of the normalized streamwise equivalent velocity, U^*_{eq}, for the cluster with normalized wind speed from 0.76 to 0.81 and *TI* between 13.5% and 19.4%. In Figure 12A, the mean velocity profiles show the typical Gaussian-like wake already detected from previous field experiments,[15,49,68] wind tunnel tests,[61,62] and numerical simulations.[69] A certain level of asymmetry in the mean velocity field is observed on the side of the wake, which might be due to the transverse variability of the incoming wind field. However, the velocity field results to be more symmetric with respect to the center within the wake. The standard deviation of the streamwise velocity, σ_U, shows two peaks in proximity of the wake boundaries, which then reduce moving in the downstream direction in agreement with previous numerical simulations[70,71] and wind tunnel experiments.[61,62]

For the characterization of the wake evolution among different clusters, the characteristic velocity deficit has been quantified through the minimum of $\overline{U_{eq}}$ for each downstream location, U^*_{min}, while three metrics have been used to quantify wake width as a function of downstream position. First, we can define the wake width with the location where $\overline{U_{eq}} = 0.5 - 0.5 \times U^*_{min}$. As second procedure, we can estimate the wake width through the application of the integral form of the streamwise momentum-deficit budget, in analogy to the Jensen model.[72] Initial wake

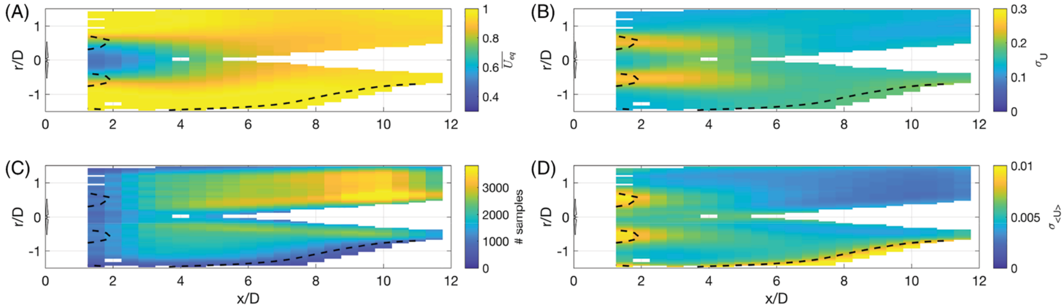

FIGURE 11 Ensemble statistics for the cluster of the light detection and ranging (LiDAR) data with $0.71 < U^*_{hub} \leq 0.76$ and $13.5\% < TI \leq 19.4\%$: A, mean normalized streamwise equivalent velocity, $\overline{U_{eq}}$; B, ensemble standard deviation, σ_U; C, number of samples per grid cell; and D, standard error of the weighted mean (SEWM). The black dashed line represents the iso-contour with SEWM equal to 0.8%

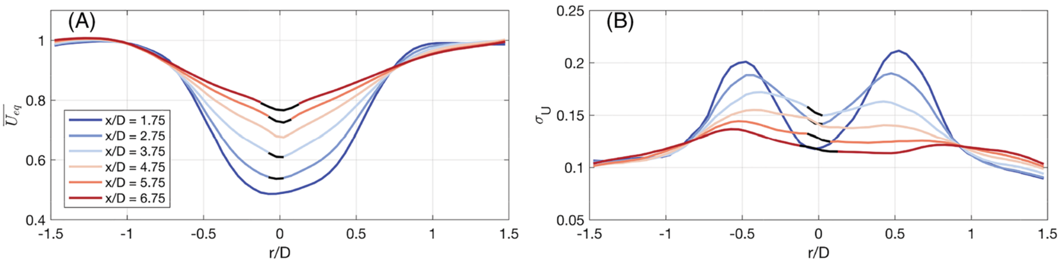

FIGURE 12 Transverse profiles of the velocity field at different downstream locations for the cluster with $0.76 < U^*_{hub} \leq 0.81$ and $13.5\% < TI \leq 19.4\%$: A, mean normalized streamwise equivalent velocity $\overline{U_{eq}}$; B, ensemble standard deviation, σ_U. Black lines represent extrapolated data

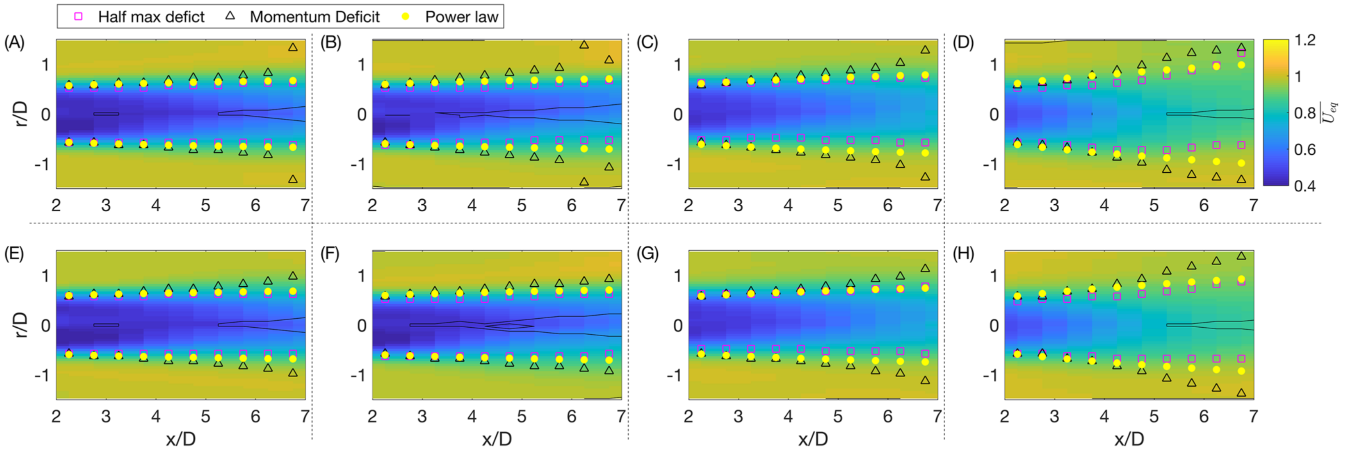

FIGURE 13 Ensemble mean velocity, $\overline{U_{eq}}$, for the clusters with $0.76 < U^*_{hub} \leq 0.80$ and different atmospheric stability regimes: A, $4\% < TI \leq 5.5\%$, B, $5.5\% < TI \leq 7\%$, C, $7\% < TI \leq 13.5\%$, D, $13.5\% < TI \leq 19.4\%$, E, $0.003 < Ri_B \leq 0.007$, F, $0.001 < Ri_B \leq 0.003$, G, $0.002 < Ri_B \leq 0.001$, and H, $-0.005 < Ri_B \leq 0.002$. Black line separates areas of measurement statistics and interpolated data

width, R_{ini}, is estimated through the first method at $x_{ini}/D = 1.75$ in order to preserve consistency among the different methods. The radius of the wake $R(x)$ must satisfy

$$\int_{-R_{ini}}^{R_{ini}} \left(1-\overline{U_{eq}}(x_{ini},r)\right) \quad |r|dr = \int_{-R(x)}^{R(x)} \left(1-\overline{U_{eq}}(x,r)\right) \quad |r|dr. \tag{16}$$

The wake half-width, R, is obtained by solving Equation (16) iteratively by gradually increasing R at a specific downstream location.

The prediction of the wake width can also be obtained through a power-law model, which has been already used from previous works for characterizing wind-turbine wakes.[3,8,73-75] Downstream variation of the mean velocity deficit can be fitted through a power law as follows:

$$U^*_{min} = 1 - A\left(\frac{x}{D}\right)^{-N}, \tag{17}$$

where A and N are parameters that should be determined from experimental data. Specifically, A is equal to the velocity deficit at $x/D = 1$ and N quantifies the wake recovery rate. In this paper, the ensemble-averaged velocity fields are leveraged to estimate the initial velocity deficit A and wake recovery rate N through a least-squares fitting. According to mass and streamwise momentum conservation, the wake width can be quantified as[75,76]

$$b_{1/2} = B\left(\frac{x}{D}\right)^{M}, \tag{18}$$

where M represents wake expansion and B is the initial wake width at $x/D = 1$. Based on mass and momentum conservation, it is found that $M = N/2$.[77]

As shown in Figures 13, 14, and 15, the three procedures to estimate the wake width agree remarkably well in the near wake. Interestingly, the wake width based on mass conservation shows a rapid expansion for $x/D \gtrsim 5$, which might be due to a less axisymmetric morphology of the wake velocity field and inclination of the PPI planes. It is noteworthy observing how the wake boundaries are practically co-located with the regions with enhanced standard deviation.

Ensemble statistics for each cluster of the LiDAR data in terms of mean and standard deviation of the streamwise velocity field are reported in the Appendix A. A comparison among ensemble statistics of clusters of the LiDAR data with normalized wind speed between 0.76 and 0.80 and

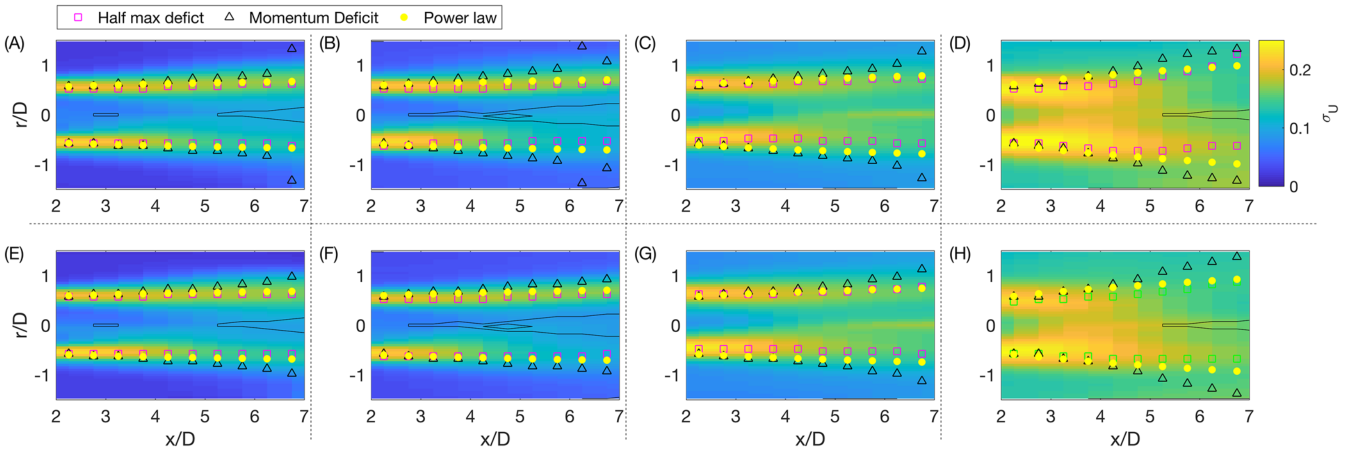

FIGURE 14 Ensemble standard deviation, σ_U, of the light detection and ranging (LiDAR) wake measurements for the clusters with $0.76 < U^*_{hub} \le 0.80$ and different atmospheric stability regimes: A, 4% < $TI \le$ 5.5%, B, 5.5% < $TI \le$ 7%, C, 7% < $TI \le$ 13.5%, D 13.5% < $TI \le$ 19.4%, E, $0.003 < Ri_B \le 0.007$, F, $0.001 < Ri_B \le 0.003$, G, $0.002 < Ri_B \le 0.001$, and H, $-0.005 < Ri_B \le 0.002$. Black line separates areas of measurement statistics and interpolated data

different atmospheric stability regimes is now presented. The respective ensemble averages are reported in Figure 13A-D when LiDAR data are clustered as a function of *TI*, while in Figure 13E-H for clusters based on Ri_B. First, effects of atmospheric stability on downstream evolution are well captured with clusters based either on *TI* or Ri_B. Specifically, as already highlighted from previous LiDAR campaigns,[8,9] enhanced turbulence intensity of the incoming wind field leads to a faster recovery of the wake velocity deficit and faster wake expansion. Furthermore, we can observe that clustering with either *TI* or Ri_B enable an effective characterization of wake variability as a function of the atmospheric stability. A quantification of the effects of atmospheric stability on wake recovery will be provided in the next section.

The analysis of the ensemble standard deviation of the velocity field also provides important information on the wake characteristics (Figure 14). As mentioned above, enhancement in σ_U is generally observed at the side boundaries of the wake followed by a downstream reduction. The regions with higher σ_U are generally narrower for stable atmospheric conditions (low *TI* or positive Ri_B), while they become more diffused for convective atmospheric conditions (higher *TI* or negative Ri_B). For convective conditions, the maximum values of σ_U also increase, indicating that on top of the wake-generated turbulence and detachment of wake vorticity structures, significant meandering oscillations are induced by the higher incoming turbulence intensity. It is interesting to observe that these ensemble statistics allow a good estimate of the incoming atmospheric turbulence as well.

Effects on wind-turbine wakes due to different incoming wind speed and, thus, different thrust coefficient of the rotor, C_t, can be observed by selecting only clusters of the LiDAR data with similar atmospheric stability regimes. Specifically, the clusters of Figure 15 are all characterized by an incoming turbulence intensity between 7% and 13.5%. Starting from the cluster in Figure 15A with relatively low incoming wind speed ($0.44 < U^*_{hub} \le 0.53$), a well-demarcated velocity deficit is observed downstream of the turbine rotor with associated regions of enhanced σ_U at the wake boundaries (Figure 15E). Increasing the incoming wind speed to the range $0.71 < U^*_{hub} \le 0.76$, the wake velocity deficit is generally increased (Figure 15B) and, as a consequence of the enhanced axial shear, the wake added turbulence intensity is also increased (Figure 15F). These wake

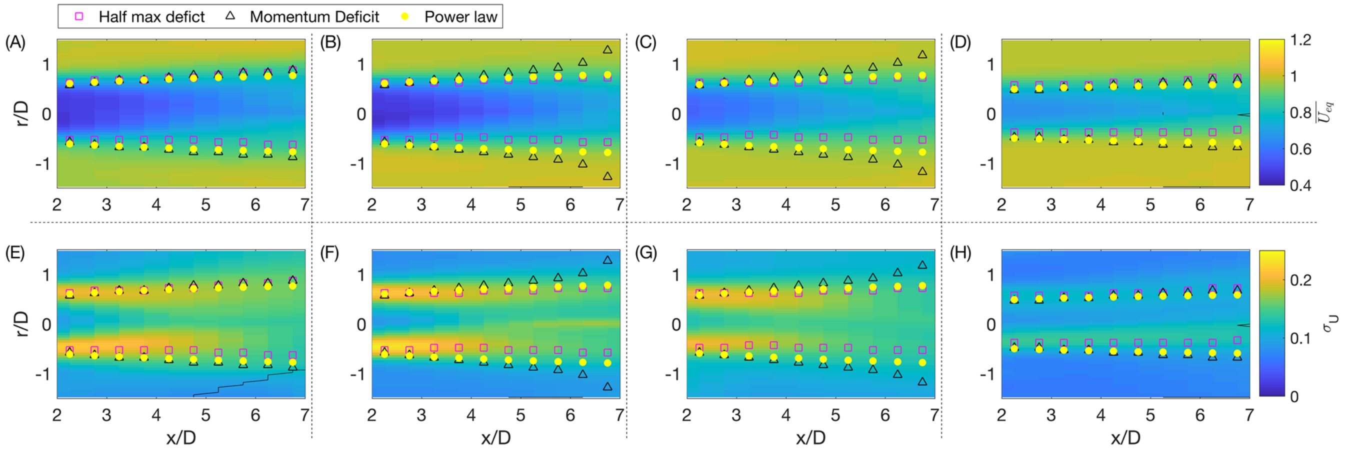

FIGURE 15 Ensemble statistic for the light detection and ranging (LiDAR)–data clusters with 7% < $TI \le$ 13.5%: A, and E, $0.44 < U^*_{hub} \le 0.53$, B, and F, $0.71 < U^*_{hub} \le 0.76$, C, and G, $0.85 < U^*_{hub} \le 0.9$, and D, and H, $1 < U^*_{hub} \le 1.04$. Ensemble mean, $\overline{U_{eq}}$, is in A, B, C, and D, while the ensemble standard deviation, σ_U, is in E, F, G, and H

features are consistent with an increased thrust coefficient, C_t, as estimated from the SCADA data and showed above in Figure 7C. For the cluster with $0.85 < U^*_{hub} \leq 0.9$, the turbine operations transition from regions 2 to 3 of the power curve by pitching the blades (Figure 7B) and leading to a reduction of C_t (Figure 7C). The transition from regions 2 to 3 of the power curve is clearly captured through the LiDAR measurements; indeed, a reduced velocity deficit and wake-generated turbulence are observed in Figure 15C,G, respectively. By further increasing the incoming wind speed to the range $1 < \overline{U^*_{hub}} \leq 1.04$ and, thus, further reducing C_t, the wake velocity deficit becomes very mild, together with a reduction of the standard deviation of the velocity at the wake boundaries.

It is noteworthy that the variation of the thrust coefficient, C_t, does not only affect the velocity deficit, but the wake width and recovery as well. Indeed, in case of a larger C_t, such as for Figure 15B, the larger velocity deficit and axial shear lead to enhanced wake-generated turbulence (Figure 15F), which promotes flow entrainment within the wake and, in turn, a faster wake recovery. In contrast, for lower C_t, such as for Figure 15D,H, even though the velocity deficit is weaker, it persists further downstream because wake diffusion mainly occurs due to the incoming atmospheric turbulence. Combined effects of atmospheric and wake-generated turbulence will be quantified in detail in the following section.

6 | MODELING WAKE RECOVERY FOR DIFFERENT INCOMING WIND SPEEDS AND ATMOSPHERIC STABILITY REGIMES

The aim of this section consists in quantifying downstream wake evolution for different turbine settings, thus C_t, and atmospheric stability regimes. For each cluster of the LiDAR dataset, the maximum ensemble-averaged velocity deficit is considered as the characteristic velocity deficit to investigate wake recovery. For the various clusters obtained with different ranges of U^*_{hub} and atmospheric stability regime, classified either through TI or Ri_B, the maximum ensemble-averaged velocity deficit is reported in Figure 16 together with the respective fitting lines obtained with the power law of Equation (17). Clusters for which the average velocity field has less than 80% of the grid points with SEWM lower than 0.8% are omitted for this analysis.

An evident increase in the slope of the fitting lines is observed by transitioning from stable to convective stability regimes, which corresponds to an increasing exponent N moving from the first column on the left-hand side of Figure 16 towards the last column at the right-hand side. This analysis corroborates results from previous LiDAR experiments performed for different atmospheric stability regimes.[8] For normalized wind speeds lower than 0.81, which correspond basically to turbine operations with constant C_t in region 2 of the power curve, the fitting lines obtained for the same stability class practically overlap. For higher wind speed, namely transitioning from regions 2 to 3 of the power curve, the increased blade pitch angle and, in turn, reduced C_t, leads to a reduction of the velocity deficit, and, as it will be shown in the following, in a reduction of the coefficient A of Equation 17. Indeed, in each panel of Figure 16, the origins of the fitting lines at the closest downstream location generally increase for darker lines, namely by reducing U^*_{hub}. Furthermore, the good agreement between the results obtained by clustering the LiDAR data as a function of TI or Ri_B suggests that variability in wake recovery induced by atmospheric turbulence is well-captured through this analysis.

In order to provide a quantitative analysis on the wake recovery for different turbine settings and atmospheric stability regimes, the fitting parameters A and N of Equation (17) obtained by clustering the LiDAR data with U^*_{hub} and TI are reported in Figure 17A, B, respectively. Parameter

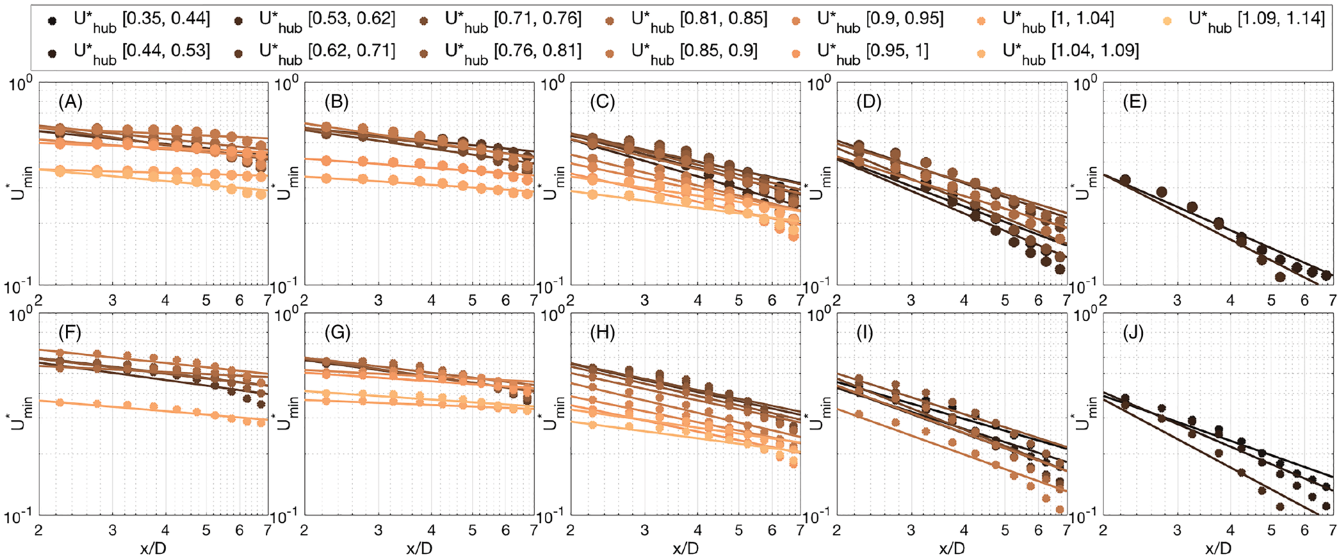

FIGURE 16 Downstream evolution of the maximum velocity deficit for different clusters of the light detection and ranging (LiDAR) data: A, 4% $< TI \leq 5.5\%$, B, 5.5% $< TI \leq 7\%$, C, 7% $< TI \leq 13.5\%$, D, 13.5% $< TI \leq 19.4\%$, E, 19.4% $< TI \leq 38.5\%$, F, $Ri_B \leq -0.005$, G, $-0.005 < Ri_B \leq -0.002$, H, $-0.002 < Ri_B \leq 0.001$, (I) $0.001 < Ri_B \leq 0.003$, and (J) $Ri_B > 0.003$. The solid lines represent fitting of the experimental data with the power law of Equation (17)

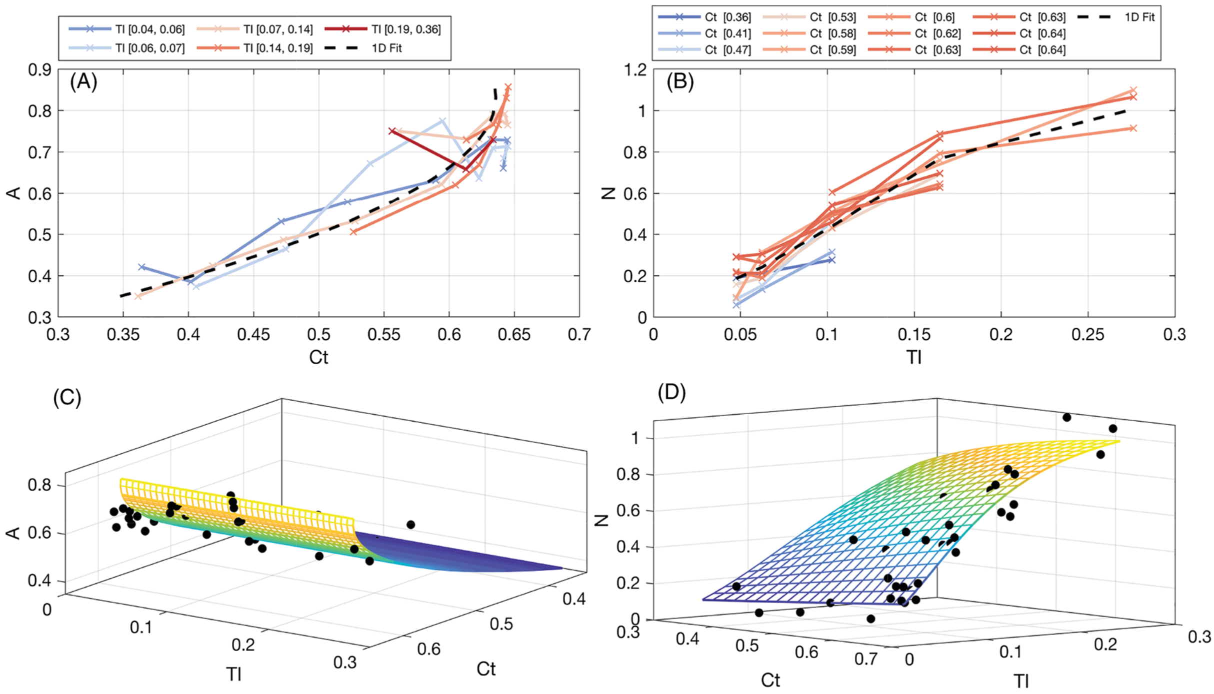

FIGURE 17 Fitting parameters for power law of Equation (17): A, A as a function of C_t, B, N as function of TI, C, A as a function of C_t and TI, and D, N as function of C_t and TI

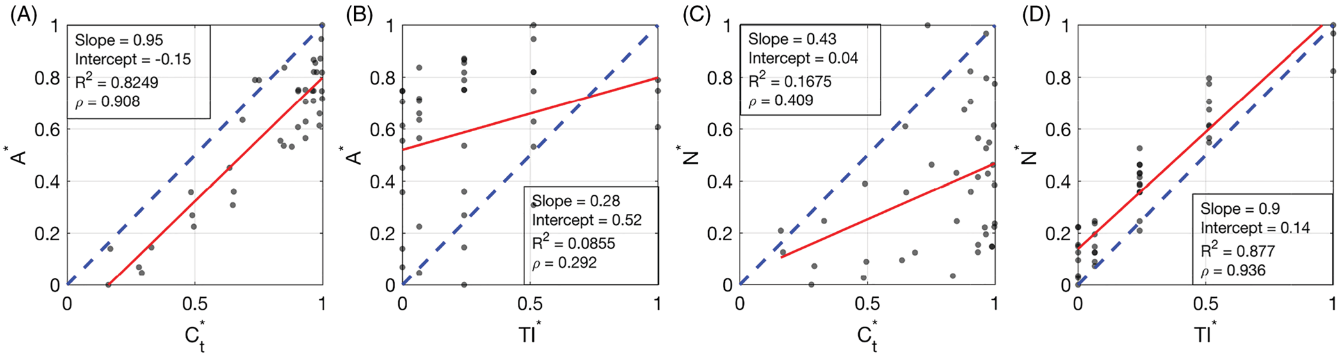

FIGURE 18 Linear regression of the normalized power-law parameters A^* and N^* with C_t^* and TI^*: A, A^* vs C_t^*, B, A^* vs TI^*, C, N^* vs C_t^*, and D, N^* vs TI^*. All the parameters are normalized with respect to their minimum and maximum values

A is related to the axial induction exerted by the turbine rotor, a.[3,75,78] By assuming a linear relationship between parameter A and the axial induction factor, a, such as $A = ka + b$, Equation (7) can be recast as follows:

$$C_t = 4\left(\frac{A-b}{k}\right)\left(1-\frac{A-b}{k}\right)+\alpha. \tag{19}$$

By fitting the values of C_t as a function of A (Figure 17A) with Equation 19, it is obtained that $k = 1.8$, $b = -0.07$, $\alpha = -0.36$, and $R-square = 0.89$, which indicates a good fitting of the experimental data with this quadratic function. By plotting parameter A as a function of C_t and TI in Figure 17C, it is observed that the dependence of A from TI is practically negligible; indeed, the experimental data have a uniform scatter around the fitting surface of Equation (19). This observation is further corroborated through the linear regression of the various parameters normalized with their respective minimum and maximum values, eg, $A^* = (A - A_{min})/(A_{max} - A_{min})$, which is reported in Figure 18. A similar normalization has been performed to generate parameters N^*, C_t^*, and TI^*. The linear regression between A^* and C_t^* produces a correlation coefficient of 0.908 with a slope of 0.95. In contrast, the linear regression between A^* and TI^* produces a correlation coefficient of 0.292 with a slope of 0.28, which confirms the negligible influence of the incoming turbulence intensity on the near-wake velocity deficit.

The rate of wake recovery, which is represented by the exponent N of Equation (17), is plotted as a function of TI in Figure 17B. As expected, an evident increase of N is observed with increasing TI representing the faster wake recovery transitioning from stable to convective atmospheric conditions. Furthermore, a secondary trend of N is observed as a function of C_t. Specifically, for a given range of TI, N slightly increases with increasing C_t. This trend is consistent with an enhanced wake recovery associated with the wake-generated turbulence, which is the result of higher C_t and velocity deficit. Indeed, by plotting N as a function of TI and C_t in in Figure 17D, it is understandable that the coupled effects of incoming and wake-generated turbulence on wake recovery rate can be modeled through a logistic function, such as

$$N = c\left(1 + e^{-\beta\left(\frac{C_t^{p_1}}{TI^{p_2}} - b\right)}\right)^{-1}. \tag{20}$$

The fitting of the experimental data with Equation (20) (R-square = 0.94) produces a growth rate $\beta = 14.824$, an inflection point $b = 0.411$, and upper asymptotic value $c = 1.1$. The exponents for C_t and TI are fitted with $p_1 = 0.273$ and $p_2 = 0.348$, respectively. It is difficult to quantify the significance of C_t and TI on the variability of N from the numerical values obtained for the coefficients p_1 and p_2. However, from the results of the linear regression between N^* vs C_t^* and TI^*, which are reported in Figure 18C,D, respectively, it is confirmed the strong dependency of N from TI (correlation coefficient of 0.936 and slope of 0.9) with a smaller, but nonnegligible, dependence from C_t with a slope of 0.43 and correlation coefficient of 0.409. This result suggests that the variation of C_t and, thus of the wake velocity deficit and shear, affects downstream wake evolution by enhancing flow entrainment within the wake, which is promoted by the increased wake-generated turbulence. Therefore, for modeling wind-turbine wakes and wind farms, it is deemed important that turbulence models should include both contributions due to the incoming atmospheric turbulence and wake-generated turbulence for reproducing accurately wake recovery.

7 | DISCUSSION AND CONCLUDING REMARKS

A LiDAR campaign was carried out for an onshore wind farm in North Texas with the aim of estimating first- and second-order statistics of the wake velocity field generated by isolated wind turbines for different turbine settings, i.e., thrust coefficient of the turbine rotor, and atmospheric stability regimes. Wind data were collected with a scanning Doppler wind LiDAR for a period between August 2015 and March 2017, together with meteorological and SCADA data. The LiDAR scanning strategy consisted of multiple narrow PPI scans probing isolated wind-turbine wakes, namely by avoiding occurrence of wake interactions. Almost 10 000 single-wake scans have been analyzed and clustered as a function of the incoming wind speed at hub height and atmospheric stability regime, which is classified through the Bulk Richardson number or incoming turbulence intensity at hub height.

Characterizing atmospheric stability for wind energy applications is not an easy task, especially considering the typical availability of meteorological data for existing power plants. The atmospheric stability condition can be characterized through the Bulk Richardson number, which provides a comparison between the two main forcing on the ABL flow, namely buoyancy and shear force, or the Obukhov length. The former requires for its calculation temperature and velocity measurements at different heights in the range of the rotor disk, while the latter needs high-frequency measurements of momentum and heat fluxes in the surface layer. In case meteorological data are not available, other engineering parameters, such as wind turbulence intensity and shear exponent, can be considered as alternative criteria to characterize the atmospheric stability regime. In this study, we have shown that a cluster analysis based on the Bulk Richardson number leads practically to the same statistical characterization of the variability of wind-turbine wakes as for a cluster analysis performed by leveraging the wind turbulence intensity at hub height. Therefore, considering that this wind parameter is often stored through the SCADA for each wind turbine for 10-minute periods, it is definitely advantageous to develop wake engineering models with parameters tuned on the incoming turbulence intensity for reproducing modulations on the wake evolution due to the atmospheric stability, as it has been proposed recently with a parabolic RANS model.[1,38]

In this paper, we provide guidelines for an accurate cluster-statistical analysis of LiDAR measurements, which are the results of an extensive experimental experience consisting of about 2-year-duration field deployment and related data post-processing. The first step for the post-processing is the overlapping of different LiDAR data collected through different scans over a common reference frame, while using consistent physical data from the various LiDAR scans. To this aim, we have shown that the quantification of the wake direction is crucial for this task and it represents the common x-direction of the used reference frame. The wake direction is estimated through a weighted linear fitting of the wake centers, which are identified through the Gaussian fitting of the wake velocity field. Each velocity field is made nondimensional through the vertical profile of the incoming wind speed, which is calculated directly from the LiDAR scan under examination and not leveraging other measurements, such as meteorological data or periodic LiDAR measurements performed with other scans, eg, Doppler beam swinging (DBS) or velocity azimuth display (VAD). This measurement strategy resulted to be instrumental to ensure a good accuracy in the statistical characterization of the wake velocity field.

In this paper, we have described in detail the calculations of the ensemble statistics from non-colocated and non-simultaneous LiDAR measurements through the Barnes scheme. Guidelines are provided for the selection of the grid-cell size, which is used for the calculation of the ensemble statistics, and radii of the weighting functions. Besides the calculation of the average velocity field, this approach enables the calculation of the standard deviation which encompasses information for the wake turbulence intensity. Obtaining turbulence statistics for non-colocated and non-simultaneous data is still a big challenge for atmospheric turbulence.[79] Furthermore, in this paper, we have proposed a parameter for quantifying accuracy in the calculation of the ensemble average, namely the SEWM. We used a threshold for the SEWM equal to 0.8% to reject data with poor statistical accuracy.

The coupled cluster-statistical analysis has enabled to single out a reduced normalized velocity deficit when wind turbine operations transition from regions 2 to 3 of the power curve as a consequence of the increased blade pitch angle and reduced thrust coefficient. Wake recovery is mainly governed by the turbulence intensity of the incoming wind; indeed, higher turbulence intensity promotes turbulent mixing and flow entrainment into the wake leading to a faster wake recovery. Furthermore, the accuracy achieved through the proposed cluster-statistical analysis has allowed detecting a secondary effect on the wake recovery rate due to the variation of the rotor thrust coefficient. A larger thrust coefficient, which is typical for operations in region 2 of the power curve aiming to maximize power capture, generates an enhanced velocity deficit and radial shear of the streamwise velocity, which is the source for a more intense mechanically-generated turbulence. This added wake-turbulence promotes wake mixing and recovery, similarly for an increase of the incoming turbulence intensity, yet with smaller impact on the wake recovery rate.

This qualitative information gathered on the variability of a turbine wake for different operative conditions and atmospheric stability regimes have been embedded in a quasi-empirical model for predictions of the maximum velocity deficit as a function of the downstream position. Downstream evolution of the maximum velocity deficit has been characterized through a power law. It has been shown that the velocity deficit in the near wake has a quadratic relationship with the turbine thrust coefficient, while it is practically independent on the turbulence intensity of the incoming wind. For the parameter of the power law representing the wake recovery rate, it can be predicted through a p-logistic function encompassing both primary dependency with incoming turbulence intensity and secondary effects related to the rotor thrust coefficient. Therefore, a simple model for predicting downstream evolution of the maximum wake velocity deficit is now available just providing incoming turbulence intensity and rotor thrust coefficient.

The various steps described in this paper for post-processing of the LiDAR data, such as use of a common reference frame and non-dimensional wind data, proper calculation of the ensemble statistics through the Barnes scheme, and quantification of the statistical accuracy, are important to single-out the physics underpinning various flow phenomena, especially in presence of complicated flow features, such as distortions and speed up induced by the site topography. We believe that these tasks for data-post-processing should be standardized through the wind energy research community in order to enable inter-comparisons among different experimental datasets and assessment of numerical models. This dataset is made publicly available.[80]

ACKNOWLEDGEMENTS

This research has been funded by a grant from the National Science Foundation CBET Fluid Dynamics, award number 1705837. This material is based upon work supported by the National Science Foundation under grant IIP-1362022 (Collaborative Research: I/UCRC for Wind Energy, Science, Technology, and Research) and from the WindSTAR I/UCRC Members: Aquanis, Inc., EDP Renewables, Bachmann Electronic Corp., GE Energy, Huntsman, Hexion, Leeward Asset Management, LLC, Pattern Energy, and TPI Composites. Any opinions, findings, and conclusions or recommendations expressed in this material are those of the authors and do not necessarily reflect the views of the sponsors. We thank the two anonymous reviewers for their constructive comments and to help improving the paper.

ORCID

Giacomo Valerio Iungo https://orcid.org/0000-0002-0990-8133

REFERENCES

1. Santhanagopalan V, Rotea MA, Iungo GV. Performance optimization of a wind turbine column for different incoming wind turbulence. *Renew Energ*. 2018;116:232-243.
2. Santhanagopalan V, Letizia S, Zhan L, Al-Hamidi LY, Iungo GV. Profitability optimization of a wind power plant performed through different optimization algorithms and a data-driven RANS solver. *Wind Energ Symp, AIAA SciTECH*. 2018;2018:2018-2018.
3. Vermeer LJ, Sørensen JN, Crespo A. Wind turbine wake aerodynamics. *Prog Arosp Sci*. 2003;39(6-7):467-510.
4. Barthelmie RJ, Hansen KS, Frandsen ST, et al. Modelling and measuring flow and wind turbine wakes in large wind farms offshore. *Wind Energ*. 2009;12(5):431-444.
5. Barthelmie RJ, Pryor SC, Frandsen ST, et al. Quantifying the impact of wind turbine wakes on power output at offshore wind farms. *J Atmos Ocean Technol*. 2010;27(8):1302-1317.
6. Nygaard NG. Wakes in very large wind farms and the effect of neighbouring wind farms. *J Phys Conf Ser*. 2014;524(1):12162.
7. Hansen KS, Barthelmie RJ, Jensen LE, Sommer A. The impact of turbulence intensity and atmospheric stability on power deficits due to wind turbine wakes at Horns Rev wind farm. *Wind Energ*. 2012;15(1):183-196.
8. Iungo GV, Porté-Agel F. Volumetric lidar scanning of wind turbine wakes under convective and neutral atmospheric stability regimes. *J Atmos Ocean Technol*. 2014;31(10):2035-2048.
9. El-Asha S, Zhan L, Iungo GV. Quantification of power losses due to wind turbine wake interactions through SCADA, meteorological and wind LiDAR data. *Wind Energ*. 2017;20(11):1823-1839.
10. Jonkman J, Butterfield S, Musial W, Scott G. Definition of a 5-MW reference wind turbine for offshore system development. National Renewable Energy Laboratory (NREL) NREL Tech Report; Golden CO; 2009.
11. Ashuri T, Martins JRRA, Zaaijer MB, Van Kuik GAM, Van Bussel GJW. Aeroservoelastic design definition of a 20 MW common research wind turbine model. *Wind Energ*. 2016;19(11):2071-2087.
12. Lundquist JK, Wilczak JM, Ashton R, et al. Assessing state-of-the-art capabilities for probing the atmospheric boundary layer: the XPIA field campaign. *Bull Americ Meteorol Soc*. 2017;98(2):289-314.

13. Debnath M, Iungo GV, Ashton R, et al. Vertical profiles of the 3-D wind velocity retrieved from multiple wind lidars performing triple range-height-indicator scans. *Atmos Meas Tech*. 2017;10(2):431-444.
14. Debnath M, Iungo GV, Brewer WA, et al. Assessment of virtual towers performed with scanning wind lidars and Ka-band radars during the XPIA experiment. *Atmos Meas Tech*. 2017;10(3):1215-1227.
15. Iungo GV, Wu Y-T, Porté-Agel F. Field measurements of wind turbine wakes with lidars. *J Atmos Ocean Technol*. 2013;30(2):274-287.
16. Iungo GV, Porté-Agel F. Measurement procedures for characterization of wind turbine wakes with scanning Doppler wind LiDARs. *Adv Sci Res*. 2013;10(1):71-75.
17. Iungo GV. Experimental characterization of wind turbine wakes: wind tunnel tests and wind LiDAR measurements. *J Wind Eng Industr Aerodyn*. 2016;149:35-39.
18. Carbajo Fuertes F, Marckfort CD, Porté-Agel F. Wind turbine wake characterization with nacelle-mounted wind lidars for analytical wake model validation. *Remote Sens*. 2018;10(5):668.
19. Käsler Y, Rahm S, Simmet R, Kühn M. Wake measurements of a multi-MW wind turbine with coherent long-range pulsed Doppler wind lidar. *Atmos Ocean Tech*. 2010;27(9):1529-1532.
20. Bingöl F, Mann J, Larsen G. Light detection and ranging measurements of wake dynamics part I: one-dimensional scanning. *Wind Energ*. 2010;13(1):51-61.
21. Trujillo JJ, Bingöl G, Larsen GC, Mann J, Kühn M. Light detection and ranging measurements of wake dynamics. Part II: two-dimensional scanning. *Wind Energ*. 2011;14(1):61-75.
22. Bastine D, Wächter M, Peinke J, Trabucchi D, Kühn M. Characterizing wake turbulence with staring lidar measurements. *J Phys Conf Ser*. 2006;625(1):12006.
23. Kumer VM, Reuder J, Svardal B, Sætre C, Eecen P. Characterisation of single wind turbine wakes with static and scanning WINTWEX-w liDAR data. *Energy Procedia*. 2015;80:245-254.
24. Clive PJ, Dinwoodie I, Quail F. Direct measurement of wind turbine wakes using remote sensing. In: Proc. EWEA; 2011. http://www.sgurrenergy.com/wp/wpcontent/uploads/2016/05/Industry-paper-Direct-measurementof-wind-turbine-wakes-using-remote-sensing.pdf
25. Wang H, Barthelmie R. Wind turbine wake detection with a single Doppler wind lidar. *J Phys Conf Ser*. 2015;625(1):12017.
26. Aubrun S, Garcia ET, Boquet M, Coupiac O, Girard N. Wind turbine wake tracking and its correlations with wind turbine monitoring sensors. Preliminary results. *J Phys Conf Ser*. 2016;753(3):32003.
27. van Dooren MF, Trabucchi D, Kühn M. A methodology for the reconstruction of 2D horizontal wind fields of wind turbine wakes based on dual-Doppler lidar measurements. *Remote Sens*. 2016;8(10):809.
28. Trujillo JJ, Seifert JK, Würth I, Schlipf D, Kühn M. Full-field assessment of wind turbine near-wake deviation in relation to yaw misalignment. *Wind Energ Sci*. 2016;1(1):41-53.
29. Bodini N, Zardi D, Lundquist JK. Three-dimensional structure of wind turbine wakes as measured by scanning lidar. *Atmos Meas Tech*. 2017;10(8):2881-2896.
30. Hirth BD, Schroeder JL, Gunter WS, Guynes JG. Measuring a utility-scale turbine wake using the TTU-ka mobile research radars. *J Atmos Ocean Technol*. 2012;29(6):765-771.
31. Hirth BD, Schroeder JL, Gunter WS, Guynes JG. Coupling Doppler radar derived wind maps with operational turbine data to document wind farm complex flows. *Wind Energ*. 2015;18(3):529-540.
32. Wharton S, Lundquist JK. Atmospheric stability affects wind turbine power collection. *Environ Res Lett*. 2012;7(1):14005.
33. Machefaux E, Larsen GC, Koblitz T, et al. An experimental and numerical study of the atmospheric stability impact on wind turbine wakes. *Wind Energ*. 2015;19(10):1785-1805.
34. Iungo GV, Letizia S, Zhan L. Quantification of the axial induction exerted by utility-scale wind turbines by coupling LiDAR measurements and RANS simulations. *J Phys Conf Ser*. 2018;1037(6):62010.
35. Churchfield MJ, Lee S, Michalakes J, Moriarty PJ. A numerical study of the effects of atmospheric and wake turbulence on wind turbine dynamics. *J Turbul*. 2012;13(14):N14.
36. Abkar M, Porté-Agel F. The effect of atmospheric stability on wind-turbine wakes: a large-eddy simulation study. *J Phys Conf Ser*. 2014;524(1):12138.
37. Abkar M, Sharifi A, Porté-Agel F. Large-eddy simulation of the diurnal variation of wake flows in a finite-size wind farm. *J Phys Conf Ser*. 2015;625(1):12031.
38. Iungo GV, Santhanagopalan V, Ciri U, et al. Solver for low-computational-cost simulations of wind turbine wakes. *Wind Energ*. 2018;21(3):184-197.
39. Reinecke PA, Durran DR. Estimating topographic blocking using a Froude number when the static stability is nonuniform. *J Atmos Sci*. 2008;65:1035-1048.
40. Barnes SLA. Technique for maximizing details in numerical weather map analysis. *J Appl Meteorol*. 1964;3(4):396-409.
41. Newsom RK, Brewer WA, Wilczak JM, Wolfe DE, Oncley SP, Lundquist JK. Validating precision estimates in horizontal wind measurements from a Doppler lidar. *Atmos Meas Tech*. 2017;10(3):1229-1240.
42. U.S. Geological Survey Website. last access on October 31, 2017, https://www.usgs.gov/
43. IEC 61400-12-1 Ed. *2.0: Wind Turbines Part 12-1: Power Performance Measurements of Electricity Producing Wind Turbines*. Geneva, Switzerland: IEC; 2015.
44. Cariou JP, Sauvage L, Thobois L, et al. Long range scanning pulsed coherent lidar for real time wind monitoring in the planetary boundary layer. In: 16th Coherent Laser Radar Conf; Long Beach, CA; 2011:148-152.
45. Larsen GC, Madsen A, Bingöl H. Dynamic wake meandering modeling. Forskningscenter Risoe. Risoe-R, No. 1607(EN), Denmark, Risø National Laboratory; 2007.
46. Larsen GC, Machefaux E, Chougule A. Wake meandering under non-neutral atmospheric stability conditions—theory and facts. *J Phys Conf Ser*. 2015;625(1):12036IOP.
47. Stull RB. An introduction to boundary layer meteorology. Vancouver, Canada: Springer Science; 1988.

48. Burton T, Sharpe D, Jenkins N, Bossanyi E. Wind Energy Handbook. New Delhi, India; 2001. LTD. ISBN 0, 471, 48997, 2.
49. Aitken ML, Banta RM, Pichugina YL, Lundquist JK. Quantifying wind turbine wake characteristics from scanning remote sensor data. *J Atmos Ocean Technol*. 2014;31(4):765-787.
50. Monin AS, Obukhov AM. Basic laws of turbulent mixing in the ground layer of the atmosphere. *Tr Geofiz Inst, Akad Nauk SSSR*. 1954;151:163-187.
51. Obukhov AM. Turbulence in an atmosphere with a non-uniform temperature. *Bound-Layer Meteor*. 1971;2:7-29.
52. Nieuwstadt FTM. The turbulent structure of the stable, nocturnal boundary layer. *J Atmos Sci*. 1984;41:2202-2216.
53. Sedefian L, Bennett E. A comparison of turbulence classification schemes. *Atmos Environ*. 1980;14(7):741-750.
54. Businger JA, Wyngaard JC, Izumi Y, Bradley EF. Flux-profile relationships in the atmospheric surface layer. *J Atmos Sci*. 1971;28(2):181-189.
55. Dyer AJ. A review of flux-profile relationships. *Bound-Layer Meteorol*. 1974;7(3):363-372.
56. Golder D. Relations among stability parameters in the surface layer. *Bound-Layer Meteorol*. 1972;3(1):47-58.
57. Panofsky HA, Tennekes H, Lenschow DH, Wyngaard JC. The characteristics of turbulent velocity components in the surface layer under convective conditions. *Bound-Layer Meteorol*. 1977;11:355-361.
58. Takeuchi K. On the structure of the turbulent field in the surface boundary layer. *J Meteor Soc Japan*. 1961;39:346-364.
59. Basu S, Porté-Agel F, Foufoula-Georgiou E, Vinuesa J-F, Pahlow M. Revisiting the local scaling hypothesis in stably stratified atmospheric boundary-layer turbulence: an integration of field and laboratory measurements with large-eddy simulations. *Bound-Layer Meteor*. 2006;119:473-500.
60. Friedrich K, Lundquist JK, Aitken M, Kalina EA, Marshall F. Stability and turbulence in the atmospheric boundary layer: a comparison of remote sensing and tower observations. *Geoph Res Let*. 2012;39(3):L03801.
61. Iungo GV, Viola F, Camarri S, Porté-Agel F, Gallaire F. Linear stability analysis of wind turbine wakes performed on wind tunnel measurements. *J Fluid Mech*. 2013;737:499-526.
62. Viola F, Iungo GV, Camarri S, Porté-Agel F, Gallaire F. Prediction of the hub vortex instability in a wind turbine wake: stability analysis with eddy-viscosity models calibrated on wind tunnel data. *J Fluid Mech*. 2014;750:R1.
63. Ashton R, Viola F, Camarri S, Gallaire F, Iungo GV. Hub vortex instability within wind turbine wakes: effects of wind turbulence, loading conditions, and blade aerodynamics. *Phys Rev Fluids*. 2016;1(7):73603.
64. Chamorro L, Porté-agel F. A wind-tunnel investigation of wind-turbine wakes: boundary-layer turbulence effects. *Bound-Layer Meteorol*. 2009;132(1):129-149.
65. Wu Y-T, Porté-agel F. Atmospheric turbulence effects on wind-turbine wakes: an LES study. *Energies*. 2012;5(12):5340-5362.
66. Santoni C, Carrasquillo K, Aernas-Navarro I, Leonardi S. Effect of tower and nacelle on the flow past a wind turbine. *Wind Energ*. 2017;20(12):1927-1939.
67. Matlab file exchange community website. updated 13 Aug 2012, https://www.mathworks.com/matlabcentral/fileexchange/4551-inpaint-nans
68. Keck E, de Maré M, Churchfield M, Lee S, Larsen G, Madsen HA. On atmospheric stability in the dynamic wake meandering model. *Wind Energ*. 2014;17(11):1689-1710.
69. Foti D, Yang X, Guala M, Sotiropoulos F. Wake meandering statistics of a model wind turbine: insights gained by large eddy simulations. *Phys Rev Fluids*. 2016;1(4):44407.
70. Abkar M, Porté-Agel F. Influence of atmospheric stability on wind-turbine wakes: a large-eddy simulation study. *Phys Fluids*. 2015;27(3):35104.
71. Troldborg N, Sorensen JN, Mikkelsen R. Numerical simulations of wake characteristics of a wind turbine in uniform inflow. *Wind Energy: An Int J Progr Appl Wind Power Convers Technol*. 2010;13(1):86-99.
72. Jensen NO. A note on wind generator interaction. Tech. Rep. Risoe., Risø National Laboratory, Roskilde, Denmark; 1983.
73. Crespo A, Hernández J. A numerical model of wind turbine wakes and wind farms. In: Proceedings: EWEC 1986; European Wind Energy Ass Conf Exhibit, Vol. 2; Rome Italy; 1986:111-115.
74. Luken E, Talmon A, Vermeulen PEJ. Evaluation of two mathematical wind turbine wake models in various types of flow. T MT-TNO Report; Netherlands; 1986.
75. Garciá L, Vatn M, Mühle F, Sætran L. Experiments in the wind turbine far wake for the evaluation of an analytical wake model. *J Phys Conf Ser*. 2017;854(1):12015.
76. Pope SB. *Turbulent flows*. Cambridge, UK: Cambridge University Press; 2000.
77. Larsen GC. A simple wake calculation procedure. Risø-m-2760, Risø National Laboratory; Roskilde, DK; 1988.
78. Swain LM. On the turbulent wake behind a body of revolution. *Proc Roy Soc London Series A*. 1929;125(799):647-659.
79. Duncan JB, Hirth BD, Schroeder JL. Doppler radar measurements of spatial turbulence intensity in the atmospheric boundary layer. *J Appl Meteorol Climat*. 2019;58(7):1535-1555.
80. Website of the Wind Fluids and Experiments (WindFluX) Laboratory at the University of Texas at Dallas. updated 31 December 2018, https://www.utdallas.edu/windflux/

How to cite this article: Zhan L, Letizia S, Iungo G V. LiDAR measurements for an onshore wind farm: Wake variability for different incoming wind speeds and atmospheric stability regimes. *Wind Energy*. 2019;1-27. https://doi.org/10.1002/we.2430

APPENDIX A: : FIRST- AND SECOND-ORDER STATISTICS OF THE WAKE VELOCITY FIELD FOR THE VARIOUS CLUSTERS OF THE LIDAR DATA

Mean velocity and standard deviation of the wake velocity fields are reported for the various clusters in two forms, namely color maps and transverse profiles at hub height for six different downstream locations. This is the list of the figures reported in the following:

- Color maps of the mean velocity field calculated for clusters based on normalized wind speed at hub height, U^*_{hub}, and turbulence intensity, *TI*, are reported in Figure A1.

- Color maps of the velocity standard deviation calculated for clusters based on normalized wind speed at hub height, U^*_{hub}, and turbulence intensity, TI, are reported in Figure A2.
- Color maps of the mean velocity field calculated for clusters based on normalized wind speed at hub height, U^*_{hub}, and Bulk Richardson number, Ri_B, are reported in Figure A3.
- Color maps of the velocity standard deviation calculated for clusters based on normalized wind speed at hub height, U^*_{hub}, and Bulk Richardson number, Ri_B, are reported in Figure A4.
- Transverse profiles at hub height of the mean velocity field calculated for clusters based on normalized wind speed at hub height, U^*_{hub}, and turbulence intensity, TI, are reported in Figure A5.

- Transverse profiles at hub height of the velocity standard deviation calculated for clusters based on normalized wind speed at hub height, U^*_{hub}, and turbulence intensity, TI, are reported in Figure A6.
- Transverse profiles at hub height of the mean velocity field calculated for clusters based on normalized wind speed at hub height, U^*_{hub}, and bulk Richardson number, Ri_B, are reported in Figure A7.
- Transverse profiles at hub height of the velocity standard deviation calculated for clusters based on normalized wind speed at hub height, U^*_{hub}, and bulk Richardson number, Ri_B, are reported in Figure A8.

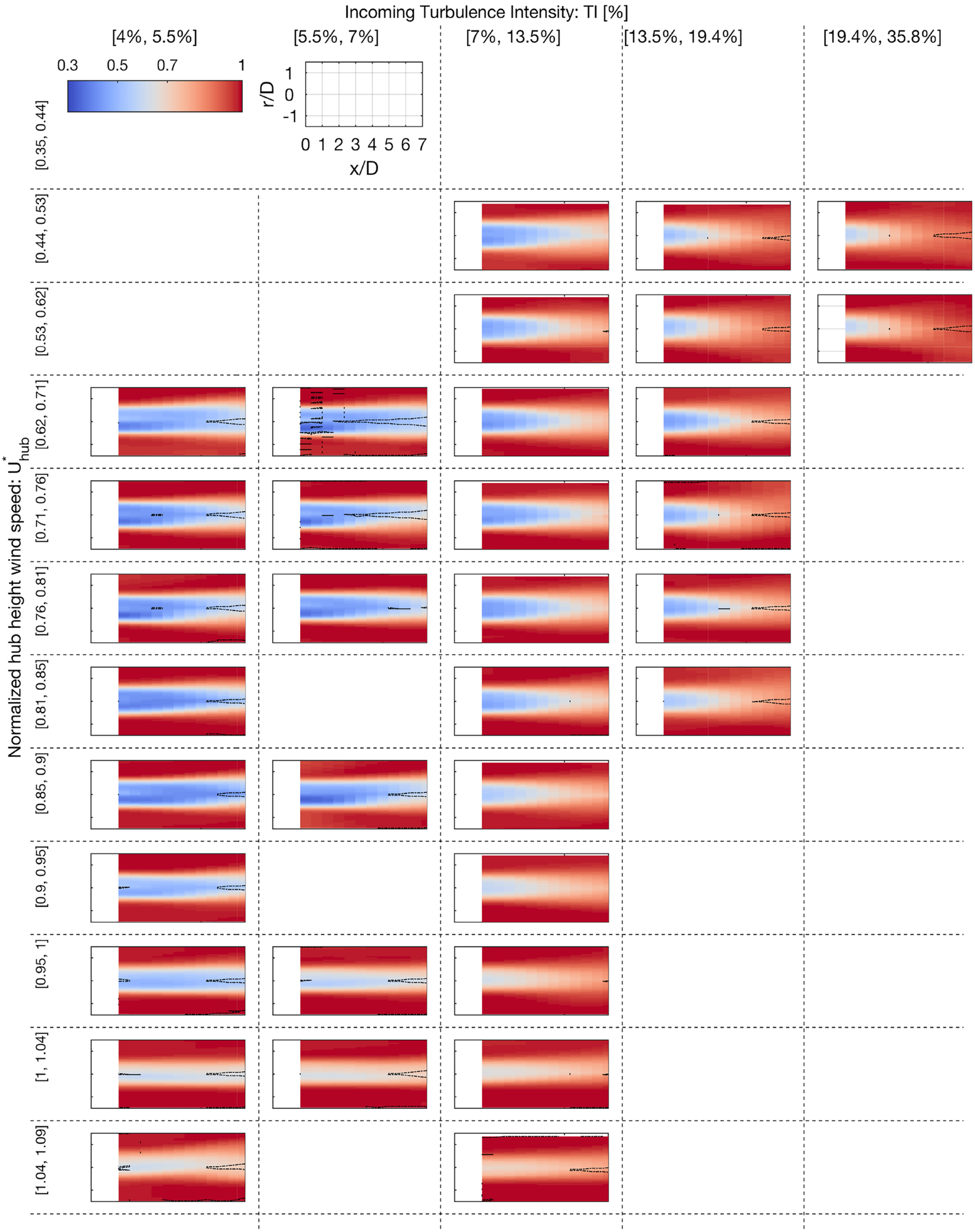

FIGURE A1 Ensemble-average of the wake velocity field, $\overline{U_{eq}}$, clustered as a function of incoming wind speed and turbulence intensity at hub height

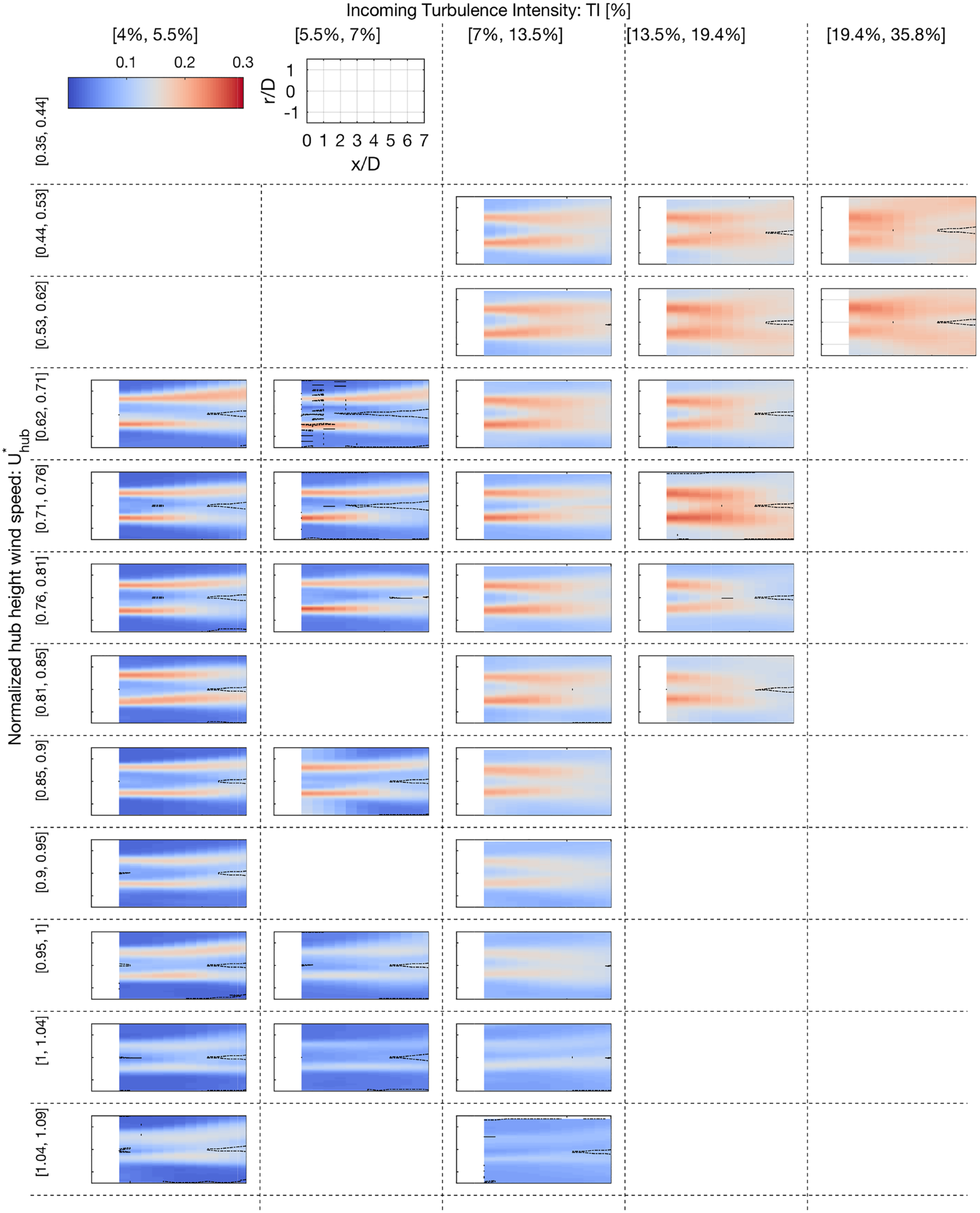

FIGURE A2 Ensemble standard deviation of the wake velocity field, σ_U, clustered as a function of incoming wind speed and turbulence intensity at hub height

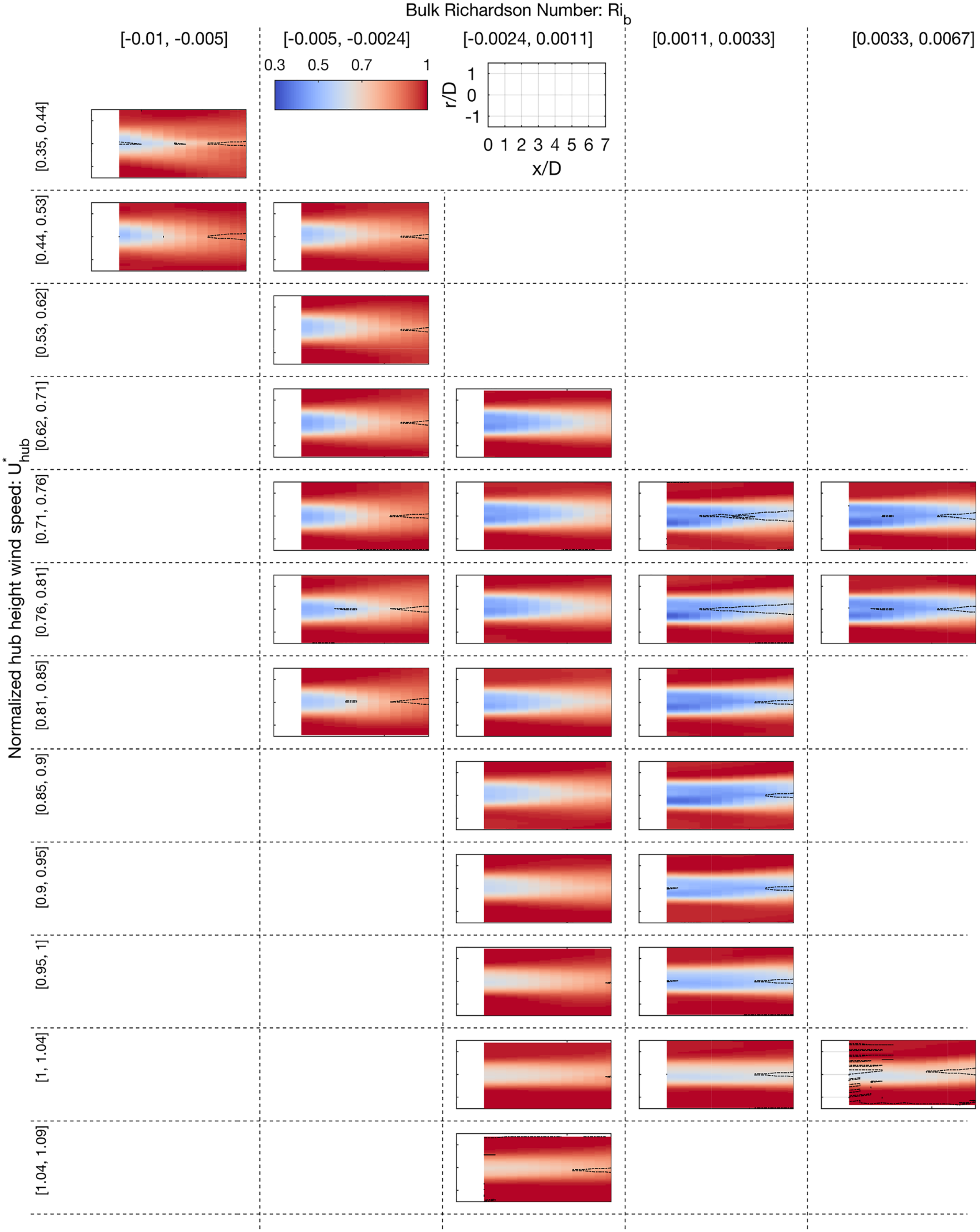

FIGURE A3 Ensemble-average of the wake velocity field clustered as a function of incoming wind speed and bulk Richardson number

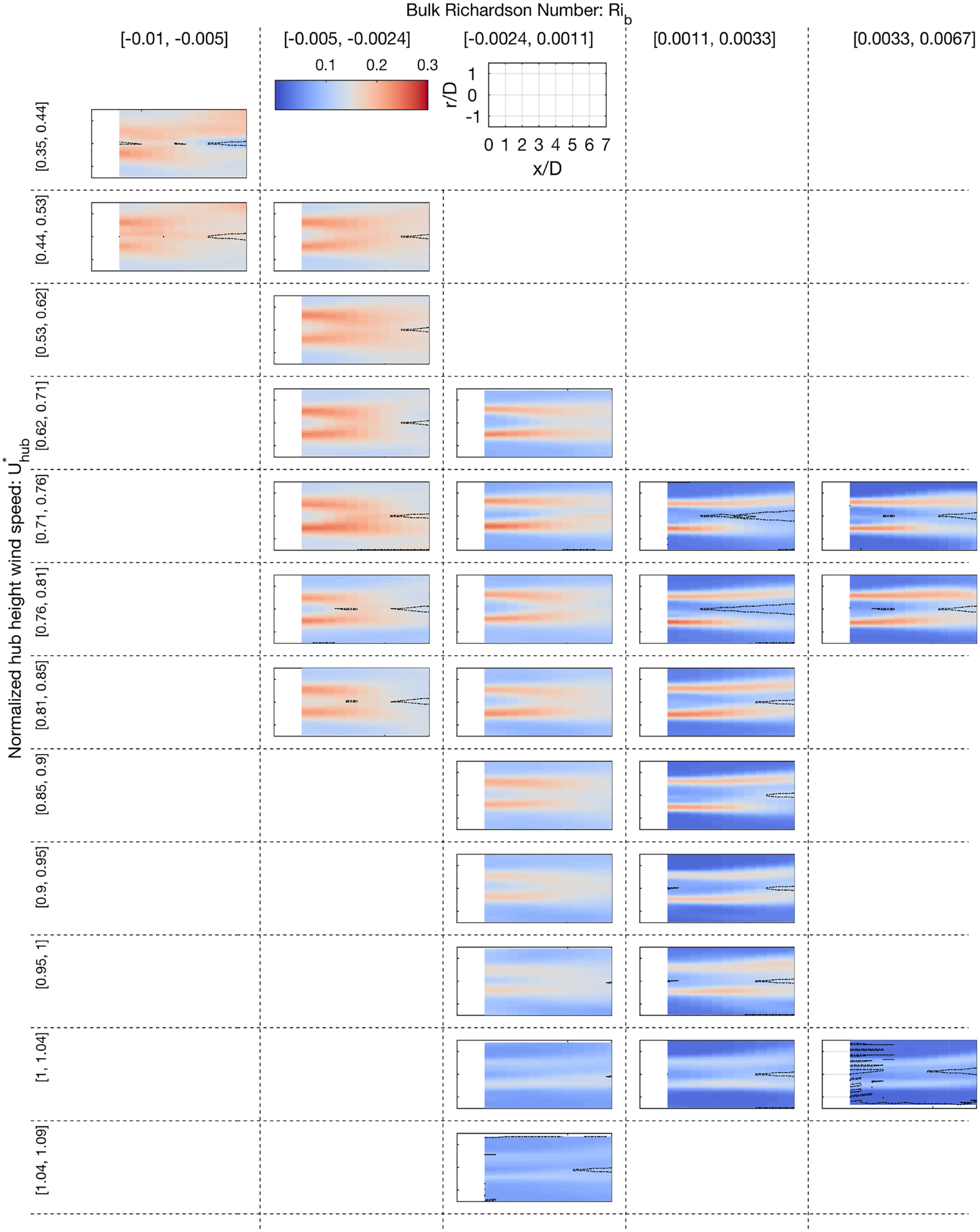

FIGURE A4 Ensemble standard deviation of the wake velocity field clustered as a function of incoming wind speed and bulk Richardson number

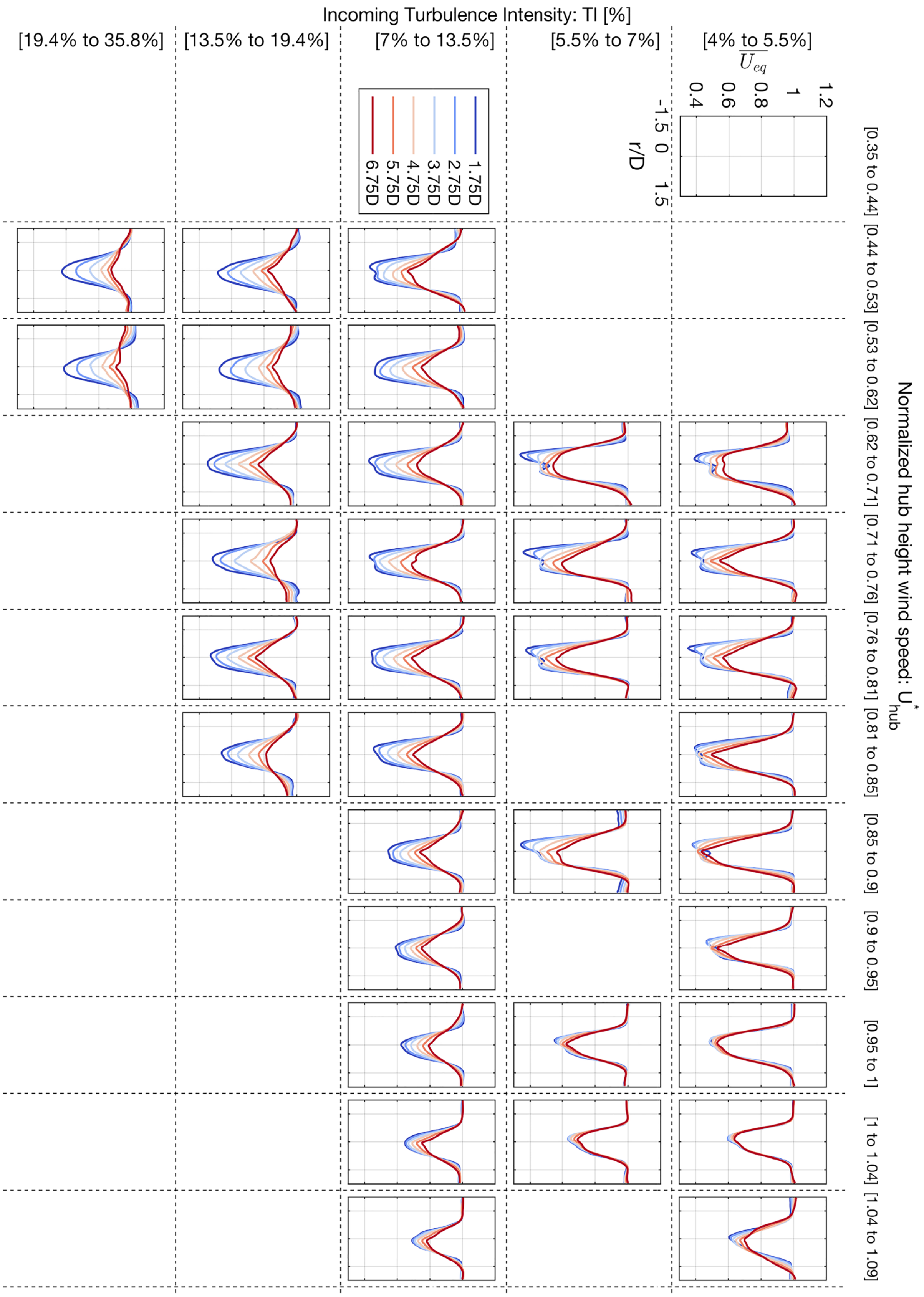

FIGURE A5 Profiles of the ensemble-average of the wake velocity field clustered as a function of incoming wind speed and turbulence intensity at hub height

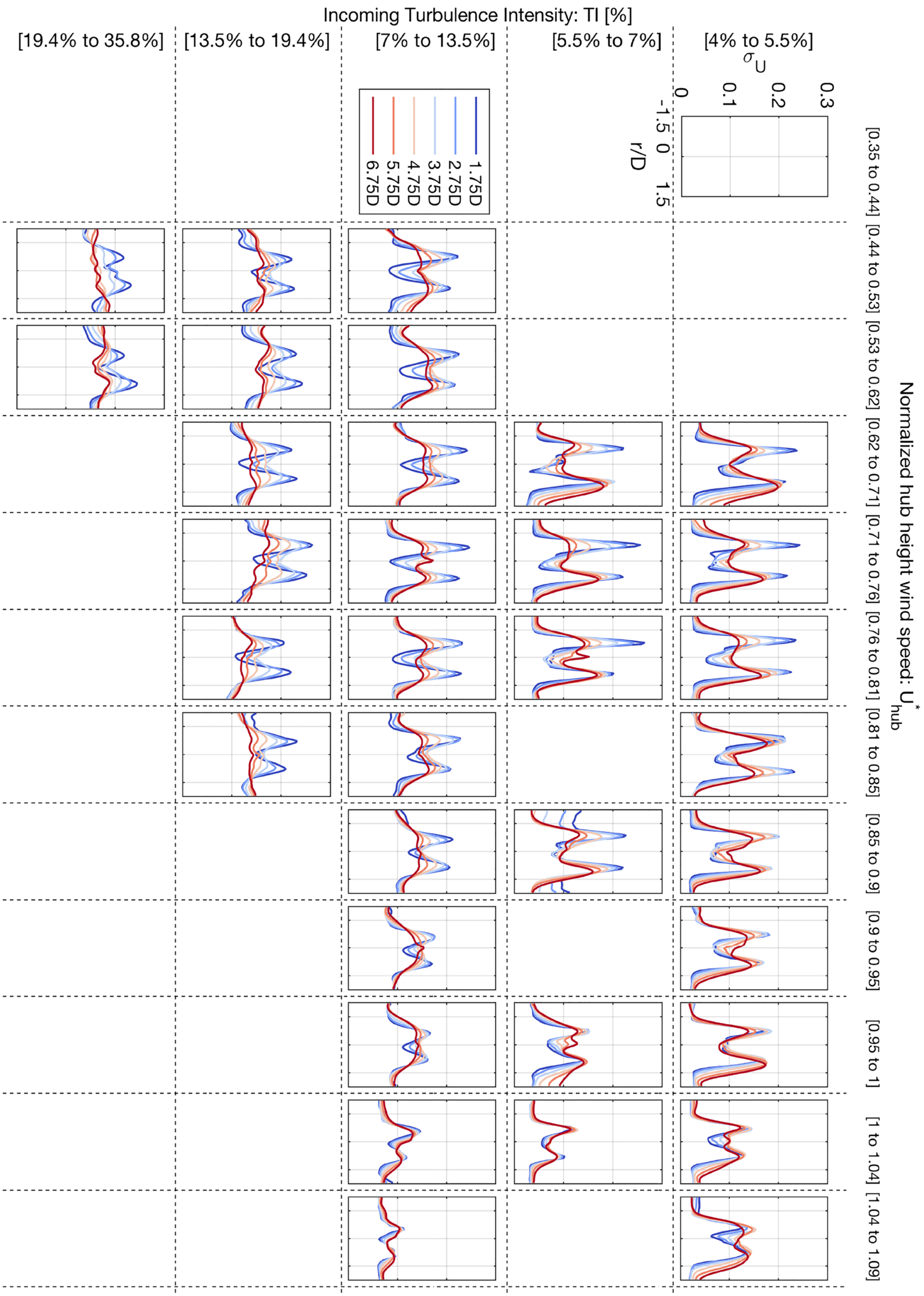

FIGURE A6 Profiles of the ensemble standard deviation of the wake velocity field clustered as a function of incoming wind speed and turbulence intensity at hub height

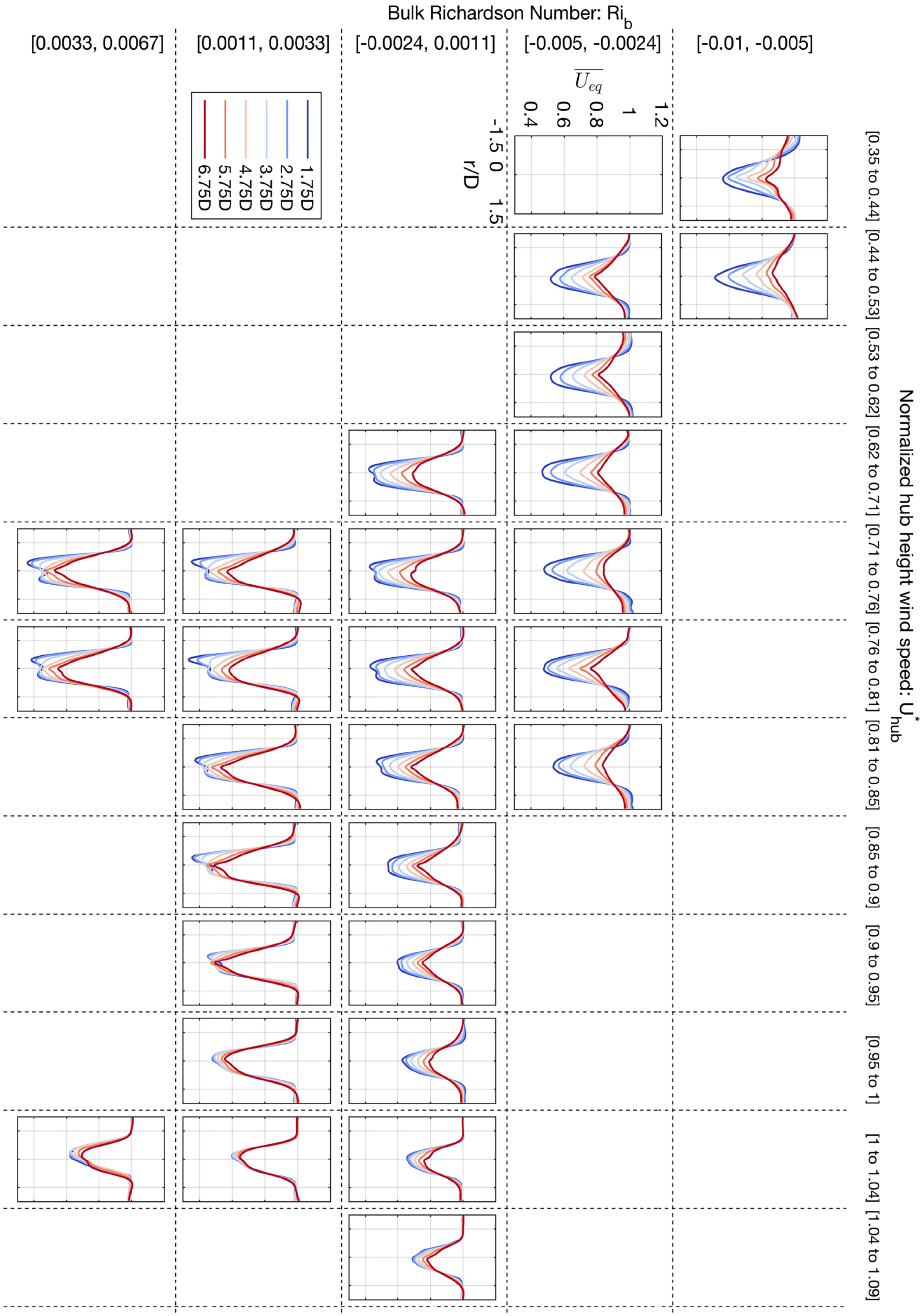

FIGURE A7 Profiles of the ensemble-average of the wake velocity field clustered as a function of incoming wind speed and bulk Richardson number

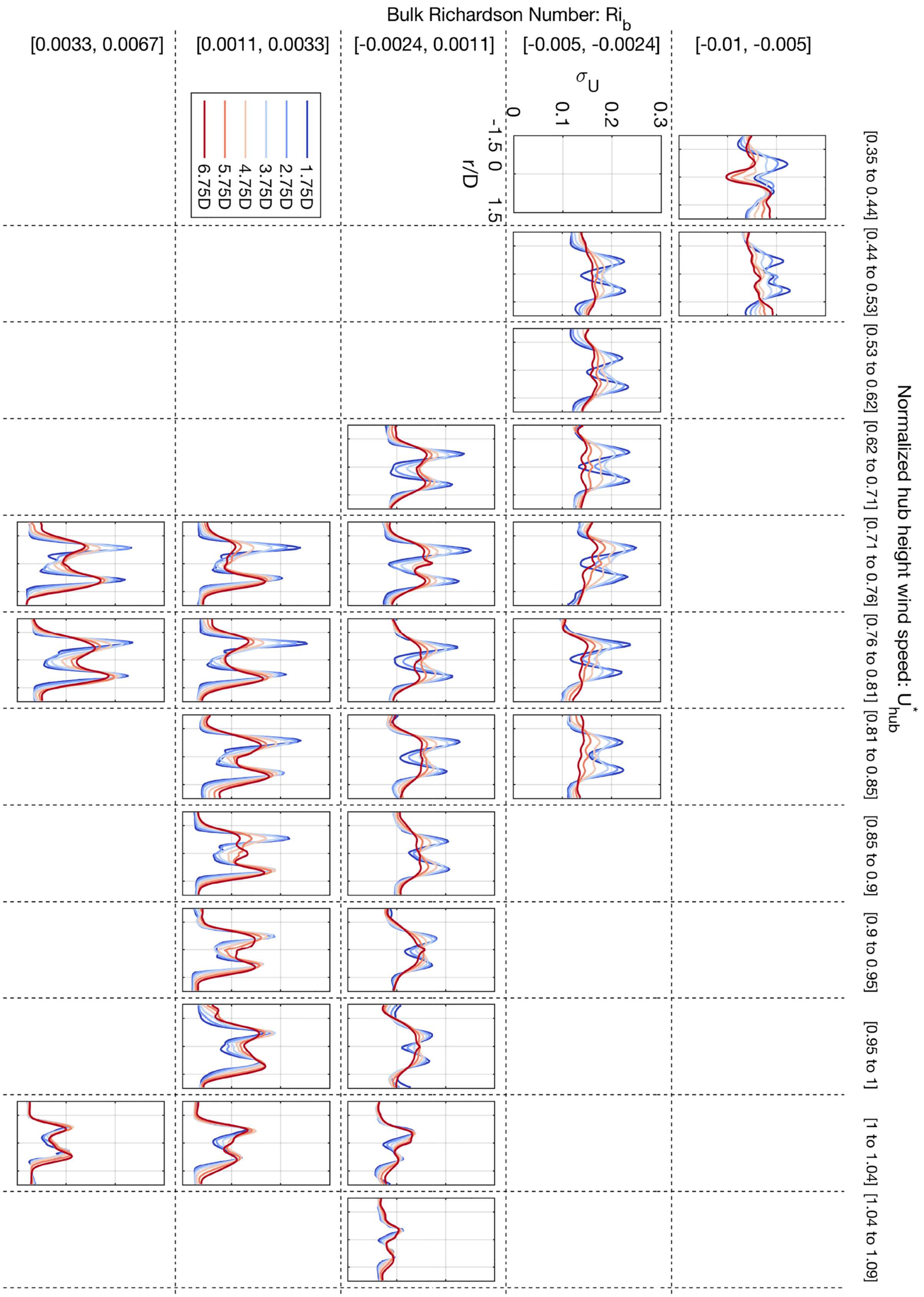

FIGURE A8 Profiles of the ensemble standard deviation of the wake velocity field clustered as a function of incoming wind speed and bulk Richardson number